

## A Composite Analysis of Snowfall Modes from Four Winter Seasons in Marquette, Michigan

CLAIRE PETTERSEN,<sup>a</sup> MARK S. KULIE,<sup>b</sup> LARRY F. BLIVEN,<sup>c</sup> ARONNE J. MERRELLI,<sup>a</sup>  
WALTER A. PETERSEN,<sup>d</sup> TIMOTHY J. WAGNER,<sup>a</sup> DAVID B. WOLFF,<sup>c</sup> AND NORMAN B. WOOD<sup>a</sup>

<sup>a</sup> *Space Science and Engineering Center, University of Wisconsin–Madison, Madison, Wisconsin*

<sup>b</sup> *Advanced Satellite Products Branch, NOAA/NESDIS/Center for Satellite Applications and Research, Madison, Wisconsin*

<sup>c</sup> *NASA Goddard Space Flight Center, Wallops Flight Facility, Wallops Island, Virginia*

<sup>d</sup> *NASA Marshall Space Flight Center, Huntsville, Alabama*

(Manuscript received 29 April 2019, in final form 15 October 2019)

### ABSTRACT


Presented are four winter seasons of data from an enhanced precipitation instrument suite based at the National Weather Service (NWS) Office in Marquette (MQT), Michigan (250–500 cm of annual snow accumulation). In 2014 the site was augmented with a Micro Rain Radar (MRR) and a Precipitation Imaging Package (PIP). MRR observations are utilized to partition large-scale synoptically driven (deep) and surface-forced (shallow) snow events. Coincident PIP and NWS MQT meteorological surface observations illustrate different characteristics with respect to snow event category. Shallow snow events are often extremely shallow, with MRR-indicated precipitation heights of less than 1500 m above ground level. Large vertical reflectivity gradients indicate efficient particle growth, and increased boundary layer turbulence inferred from observations of spectral width implies increased aggregation in shallow snow events. Shallow snow events occur 2 times as often as deep events; however, both categories contribute approximately equally to estimated annual accumulation. PIP measurements reveal distinct regime-dependent snow microphysical differences, with shallow snow events having broader particle size distributions and comparatively fewer small particles and deep snow events having narrower particle size distributions and comparatively more small particles. In addition, coincident surface meteorological measurements indicate that most shallow snow events are associated with surface winds originating from the northwest (over Lake Superior), cold temperatures, and relatively high surface pressures, which are characteristics that are consistent with cold-air outbreaks. Deep snow events have meteorologically distinct conditions that are accordant with midlatitude cyclones and frontal structures, with mostly southwest surface winds, warmer temperatures approaching freezing, and lower surface pressures.

## 1. Introduction


The Laurentian Great Lakes region of North America is a Canadian–American expanse home to approximately 60 million people and encompasses large urban and rural areas. The Great Lakes have a huge impact on the

surrounding regional weather and climate (Sousounis and Fritsch 1994; Angel and Isard 1998; Sousounis and Mann 2000; Notaro et al. 2013), with one of the most prominent features being frequent snow events during the cold season (Peace and Sykes 1966; Eichenlaub 1979; Niziol et al. 1995). The region is highly affected by snowfall through socioeconomic impacts (Changnon 1979; Schmidlin 1993; Kunkel et al. 2002), regional ecology (Norton and Bolsenga 1993; Henne et al. 2007), and hydrological planning (Burnett et al. 2003; Kolka et al. 2010). Snowfall in the Great Lakes primarily comprises two distinct formation mechanisms: 1) large-scale, synoptically driven snowfall that tends to be vertically deep and spatially expansive (Leathers and Ellis 1996; Serreze et al. 1998) and 2) surface-driven convective lake-effect snowfall (Eichenlaub 1979;

---

 Denotes content that is immediately available upon publication as open access.

---

 Supplemental information related to this paper is available at the Journals Online website: <https://doi.org/10.1175/JAMC-D-19-0099.s1>.

---

*Corresponding author:* Claire Pettersen, [claire.pettersen@ssec.wisc.edu](mailto:claire.pettersen@ssec.wisc.edu)

DOI: 10.1175/JAMC-D-19-0099.1

© 2020 American Meteorological Society. For information regarding reuse of this content and general copyright information, consult the [AMS Copyright Policy](https://www.ametsoc.org/PUBSReuseLicenses) ([www.ametsoc.org/PUBSReuseLicenses](https://www.ametsoc.org/PUBSReuseLicenses)).

Kristovich 1993; Niziol et al. 1995), which is produced by cold-air outbreaks over the relatively warm lake surfaces and is vertically shallow with highly variable spatial impacts (Agee and Hart 1990; Niziol et al. 1995; Kristovich et al. 2017). Individual lake-effect snow (LES) events can produce localized large amounts of accumulation (Wiggin 1950; Peace and Sykes 1966; Niziol 1987), and much of the downwind shores of the Great Lakes receives greater than 2 m of snow accumulation per year on average (Eichenlaub 1979; Braham and Dungey 1984).

While the joint U.S.–Canada operational radar network and latest generation operational geostationary satellites provide valuable remote sensing observations for Great Lakes LES monitoring and nowcasting purposes, both ground-based scanning radars and spaceborne remote sensing instruments suffer from limited near-surface observational capabilities (Niziol et al. 1995; Brown et al. 2007; Smalley et al. 2017). Spaceborne radars have successfully mapped snowfall regimes, including shallow convective lake/ocean-effect snow, on a global basis (i.e., Kulie et al. 2016; Kulie and Milani 2018), but “blind zones” and/or radar sensitivity issues adversely impact their ability to observe near-surface features (Kulie et al. 2010; Skofronick-Jackson et al. 2013; Maahn et al. 2014; Skofronick-Jackson et al. 2015; Casella et al. 2017). Sustained remote sensing and in situ observations strategically focused on near-surface features to augment current observational capabilities are needed. Such observations increase our understanding of the near-surface properties and physical processes operating within different snowfall regimes, enable more accurate space-based quantitative snowfall estimates, and improve numerical models that are prone to large accumulation uncertainties due to various physical parameterizations (Sousounis et al. 1999; Reeves and Dawson 2013; Conrick et al. 2015).

There have been several successfully executed field campaigns aimed to better characterize LES events (i.e., Braham 1990; Kristovich et al. 2000; Wood et al. 2015; Skofronick-Jackson et al. 2015; Kristovich et al. 2017). The majority of these campaigns have focused on the lower Great Lakes, especially Lake Ontario, because of the intensity of LES events in this region (Niziol 1987; Kristovich et al. 2017). Many of the field experiments in the Great Lakes region focused on snowfall were only deployed for one winter season (Wood et al. 2015; Skofronick-Jackson et al. 2015; Kristovich et al. 2017). As a result, there is a dearth of observations of LES events in the upper Great Lakes for multiple winter seasons. The present work addresses these issues by providing near-continuous observations of Lake Superior snow events. Unlike previous Great

Lakes region snow experiments, this work focuses on snowfall related to Lake Superior and is a multi-season study in operation since January 2014.

Presented here is an application of a unique dataset of four winter seasons (i.e., cold season: November–April) of observations from a ground-based, vertically pointing Micro Rain Radar. This radar is used to partition all snowfall events from the four winters into two categories based on the reflectivity profile: either deep or shallow. Ancillary data from surface-based measurements of temperature, wind speed, and wind direction are used in conjunction with reanalysis products to identify distinct meteorological states for each snow category. Additionally, analysis of the radar profile characteristics and data from a collocated precipitation imager allows specific microphysical properties distinguishing deep versus shallow snow events to be investigated. Section 2 describes the site instrumentation and data methods employed for this analysis. Section 3 details the radar-based partitioning approach used to categorize the snow events. Section 4 examines characteristics of each snow category using ancillary surface-based measurements and reanalysis products. Section 5 outlines future plans for and further applications of this unique dataset.

## 2. Site, instrumentation, and data methods

### a. Deployment site

The instrumentation suite was installed in January 2014 at the Marquette, Michigan (MQT), National Weather Service (NWS) Office, which is 13 km inland from Lake Superior on terrain with a gradual slope rising more than 200 m above the lake shore (46.53°N, 87.55°W, 426 m above sea level; Fig. 1, right). This site was chosen for several reasons: first, the NWS office is an ideal location for observations as this area receives approximately 250 to 500 cm of measured snow accumulation per year. Second, the reliable power and Internet connectivity at the NWS office enables a high percentage of uptime (>97% over 5 years), continuous remote access to instruments for analysis and maintenance, real-time transfer of data, and the ability to generate daily figures on a public website ([https://www.ssec.wisc.edu/lake\\_effect/mqt/](https://www.ssec.wisc.edu/lake_effect/mqt/)). Additionally, it is continuously staffed by technicians and meteorologists who have graciously lent their expertise and time to this project, and are, in large part, the reason this deployment has been successful in obtaining continuous data since the start of the campaign. Last, the collocated weather radar, surface meteorological data, snowfall accumulation measurements, and forecaster observations are invaluable resources used to create a unique merged dataset.

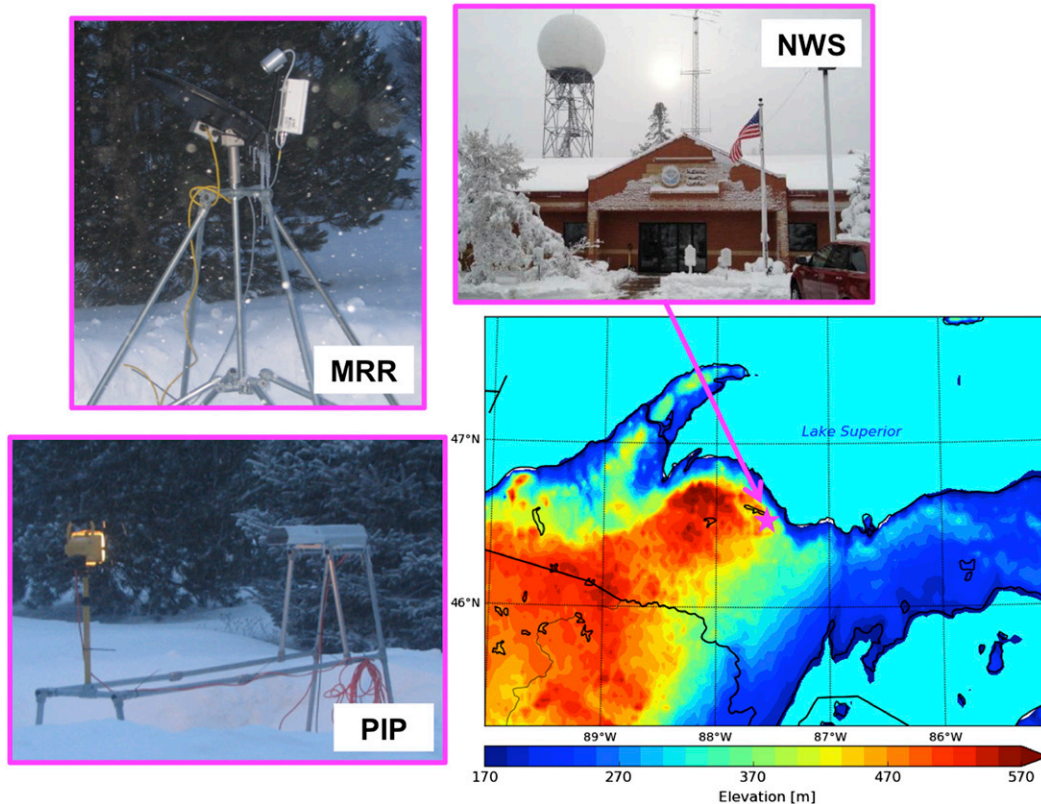


FIG. 1. (bottom right) The location of the instrument suite at the Marquette (MQT) NWS Office (indicated by the magenta star), along with the topography of the surrounding area near the NWS MQT office. In addition to observations from (top right) the NWS office, we use profile information from (top left) an MRR and (bottom left) surface measurements from a PIP. The instruments at the site are all located within 10 m of each other.

## b. Instrumentation

### 1) PRECIPITATION PROFILING RADAR

The METEK Micro Rain Radar 2 (MRR) is a vertically profiling, 24-GHz (K band) frequency-modulated, continuous-wave Doppler radar (Klugmann et al. 1996). The MRR has been successfully used in field campaign observations of both rain (i.e., Peters et al. 2002; Rollenbeck et al. 2007) and snow (i.e., Kneifel et al. 2011; Maahn and Kollias 2012; Skofronick-Jackson et al. 2015; Minder et al. 2015; Kristovich et al. 2017). The MRR is small and easily deployable, ideal for fieldwork (Klugmann et al. 1996). Figure 1 illustrates the footprint of the MRR at the NWS MQT site. The antenna dish is 0.5 m in diameter and is mounted  $\sim 2$  m above the ground. The transmitter is low power (50 mW) and requires only 25 W while operating (the dish heater that is required during winter months adds 500 W). The MRR at the NWS MQT site is configured to profile up to 3000 m above ground level (AGL) in 30 fixed range gates, with a vertical resolution of 100 m. This profile range

allows for distinguishing shallow from deep snowfall events while retaining high enough vertical resolution to examine microphysical characteristics (Kneifel et al. 2011). The raw data output includes measurements of reflectivity factor (hereafter, reflectivity), Doppler velocity, and spectral width at 1-min resolution. Because of ground clutter, we remove the first three range gates of MRR observations with the closest surface observations originating at 400 m AGL. We apply the Matrosov (2007) radar reflectivity factor  $Z$  to snowfall rate  $S$  relationship to the MRR reflectivity to obtain a snowfall rate:

$$Ze = 56S^{1.2}, \quad (1)$$

with sensitivity of  $0.01 \text{ mm h}^{-1}$  [liquid water equivalent (LWE)]. This relationship has been used to estimate snowfall accumulation from profiling radars in several studies (Kneifel et al. 2011; Maahn and Kollias 2012; Castellani et al. 2015; Pettersen et al. 2018). The raw power spectra data are optimized for snowfall observations using the Maahn and Kollias (2012) method described in section 2d.

TABLE 1. Detailed specifications for the surface meteorological observations used from the Davis Vantage Pro2 (note that 1 kt  $\approx$  0.51 m s<sup>-1</sup>).

Measurement	Sensor	Range	Resolution	Accuracy
Temperature	“PN” junction silicon diode	From $-40^{\circ}$ to $+65^{\circ}\text{C}$	0.1°C	$\pm 0.3^{\circ}\text{C}$
Relative humidity	Film capacitor element	1%–100%	1%	$\pm 2\%$
Wind speed	Solid-state magnetic sensor	0–173 kt	1 kt	$\pm 2$ kt
Wind direction	Wind vane with a potentiometer	$1^{\circ}$ – $360^{\circ}$	$1^{\circ}$	$\pm 3^{\circ}$
Surface pressure	Barometric sensor	1100–540 hPa	0.1 hPa	$\pm 1$ hPa

## 2) WEATHER RADAR

The NWS MQT office is part of the Next Generation Weather Radar (NEXRAD) network and has an S-band Weather Surveillance Radar-1988 (WSR-88D). Level II and III data products for the NEXRAD system are available through the National Oceanic and Atmospheric Administration (NOAA) National Center for Environmental Information (NCEI) archive. In this work, we use the base reflectivity and volume coverage pattern (VCP) information from the Level II data. During the winter months, the MQT WSR-88D operates mostly in the VCP 32 (clear air mode, five elevation scans with a maximum elevation angle of  $4.3^{\circ}$ ) or in the VCP 221 (precipitation mode, nine elevation scans with a maximum elevation angle of  $19.5^{\circ}$ ) scanning configuration. We use the NEXRAD Level III data to examine the precipitation enhanced echo-top (EET) heights during snow events. The EET is computed within a VCP by using the maximum elevation angle and determining the height (AGL) at which reflectivities of  $\geq +18$  dBZ are detected.

## 3) PRECIPITATION IMAGER

The Precipitation Imaging Package (PIP) is a NASA-developed video disdrometer, which evolved from the Snowflake Video Imager (Newman et al. 2009; Tiira et al. 2016). The PIP consists of a high-speed video camera (380 frames per second) with a 640 by 480 pixel charge-coupled device image sensor. This camera is aimed at a bright (150 W) halogen lamp at 2-m distance. The PIP is calibrated such that the field of view is 64 mm by 48 mm and the focal plane is located 1.33 m from the lens. The PIP image resolution is approximately 0.1 mm by 0.1 mm. The PIP setup is unique in that precipitation particles are comparatively unimpeded by the instrument itself, as the design provides an open volume between the camera and the lamp (see Fig. 1, lower left; Newman et al. 2009). Hydrometeor shadows are recorded as they fall through the observation volume and used to calculate particle size distributions (PSDs) and fall speed estimates with 1-min resolution (Newman et al. 2009; Tiira et al. 2016; von Lerber et al. 2018).

Advancements in computer processing capabilities and expanded software enable the PIP to provide additional

capabilities such as phase-separated rain and snow rate estimates (Tiira et al. 2016; von Lerber et al. 2018). The PIP software uses observations of PSD and fall velocities in conjunction with an empirically derived parameterization of effective density as a function of particle diameter to both phase separate the rain and snow events and acquire precipitation rates.

## 4) SURFACE METEOROLOGICAL OBSERVATIONS

The surface meteorological data are obtained from the automated Davis Vantage Pro2 weather station (Davis Instruments 2018), which is mounted on a tower (10 m AGL) adjacent to the NWS office. Measurements of the surface temperature, relative humidity (RH), wind speed, wind direction, and pressure are used in this study (instrument specifications outlined in Table 1). All observations are reported at 1-min intervals.

## 5) SNOW FIELD OBSERVATIONS

The snow field at the NWS MQT office consists of four 150-cm snow stakes evenly distributed across a flat and open parcel of land approximately 36 m<sup>2</sup> in area. The snowpack depth is the average taken from these four snow stakes. The new snow accumulations are taken using a plastic, white snow board every six hours (0000, 0600, 1200, and 1800 UTC) during snow events. The plastic board is placed adjacent to the snow stake field and is cleared off after each measurement. LWE snowfall amounts are also taken every 6 h in coordination with the snow-board measurements. To obtain LWE snow accumulation, a 20.32-cm-diameter standard rain gauge (SRG) is used. Snow from the SRG is melted to convert from geometric to LWE accumulation. All snow accumulation observations from the MQT snow field are obtained by NWS meteorologists.

### c. Reanalysis products

This study examines temperature and RH products from the ERA5 reanalysis dataset (C3S 2017). The ERA5 products are available every 1 h from 1979 through the present and have a horizontal spatial resolution of 31 km



(globally) and 137 vertical layers to 0.01 hPa. This study employs the grid point closest to the site: 46.5°N, 87.5°W.

#### d. Radar data methods

Past snowfall studies indicate good agreement between the MRR and a 35-GHz cloud profiling radar when reflectivities were greater than 3 dBZ (Kneifel et al. 2011). However, global snowfall frequently occurs below this value (Kulie and Bennartz 2009). To help resolve the MRR detection of light snow and precipitation, Maahn and Kollias (2012; hereinafter MK12) developed a method to increase the MRR sensitivity by postprocessing the MRR spectra to remove signals from range gates with no hydrometeors, as well as determine the most significant peak and classify the remaining spectrum as noise, effectively improving observations of light precipitation to approximately  $-10$  dBZ. Consequently, the MK12 algorithm for enhanced MRR snowfall detection is applied to the observations in this study.

An additional issue specific to the MQT site is intermittent interference. We hypothesize that this interference may be due to a nearby ( $<200$ -m distance) television-broadcasting tower. When examining the raw power spectra from the MRR, the interference appears as a regular repeated pattern, distinct from any precipitation signal. A principal component analysis (PCA) was applied to the MRR raw power spectra to isolate and remove the corrupted time samples (see section S.1 in the online supplemental material for details). Several tests were applied during both clear-sky and varying precipitation conditions to ensure that no valid observations were lost due to the application of the PCA filter. More detailed information on filtering the interference can be found in the accompanying supplemental documentation.

#### e. Statistical methods

We used two methods of testing the significance of differences of the characteristics of the deep and shallow snowfall: difference of means and blocked bootstrap. To test the significance of the difference between two independent sample means, we use

$$z = \frac{\bar{x}_1 - \bar{x}_2}{\left(\frac{s_1^2}{N_1} + \frac{s_2^2}{N_2}\right)^{1/2}}, \quad (2)$$

where  $\bar{x}$  is the sample mean,  $s$  is the sample standard deviation, and  $N$  is the effective sample size (Wilks 2011). Because our dataset has potential for correlation from observations occurring within the same or adjacent precipitation events, we computed independent sample

sizes by examining independent precipitation events of each type that were at least 3 h long and occur on separate days to limit overconfidence in the statistical tests. To assess the statistical significance of the difference for the PIP data, a block bootstrap random resampling was performed on the pooled dataset. We computed 5000 random resamples equal in size to the snowfall event datasets and computed the difference in the PIP data for each grouping. Because the individual 1-min sampled PSDs have significant time correlation, the samples were drawn with blocked groups of 360 samples to ensure that the confidence interval is not biased or too narrow (Wilks 2011; Henderson et al. 2016). The block size roughly divides the data into an equivalent number of “independent precipitation events,” similar to the effective  $N$  used for the difference in means tests above. For all data in this work, differences are considered to be statistically significant at a confidence level of 95%.

#### f. Final data product

All observations from the MRR for the 2014–18 winter seasons are merged with ancillary data. Coincident measurements and products from the PIP and surface meteorological instrumentation are merged to a common temporal grid with MRR observations. Additionally, the ERA5 (hourly) products and snow field measurements (6 hourly) are merged into the dataset at their respective time resolutions. Available WSR-88D Level III products of precipitation echo-top heights are added to the merged data product at the nearest time to the native resolution of the weather radar.

### 3. MRR partitioning approach

The MRR has successfully illustrated precipitation characteristics associated with distinct meteorological conditions (i.e., Stark et al. 2013; Maahn et al. 2014; Skofronick-Jackson et al. 2015; Gorodetskaya et al. 2015; Minder et al. 2015; Kristovich et al. 2017; Souverijns et al. 2017, 2018; Schirle et al. 2019). Several of these studies utilized surface and profile meteorological observations, weather forecasts, and reanalyses to diagnose the environment that produced snowfall (Stark et al. 2013; Gorodetskaya et al. 2014, 2015). In some studies, snow events were then grouped by conditions (i.e., frontal, cyclonic, or LES), and the associated MRR observations, along with other remote sensing instruments, were utilized to examine the cloud and precipitation microphysical properties (Maahn et al. 2014; Minder et al. 2015; Kristovich et al. 2017; von Lerber et al. 2018). However, many of these investigations

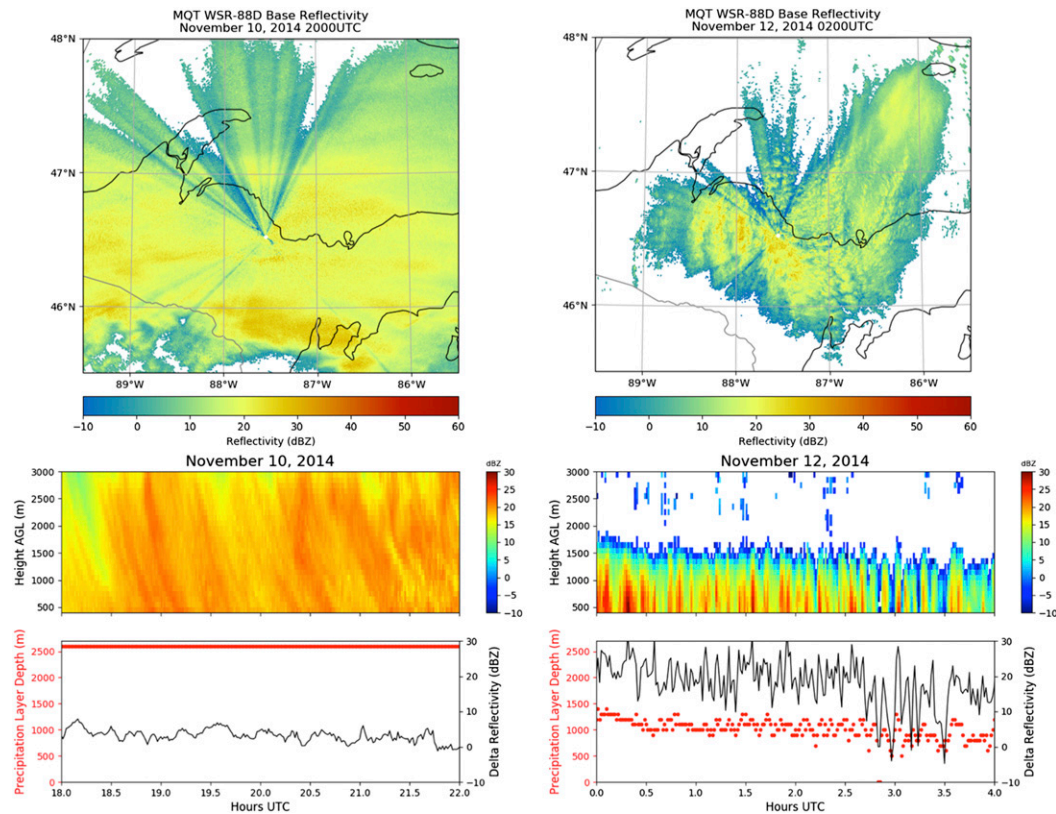


FIG. 2. Examples from two distinct snow event types: (left) a deep, system snow event (1800–2200 UTC 10 Nov 2014) and (right) a lake-effect snow event (0000–0400 UTC 12 Nov 2014), showing (top) the base reflectivity from the WSR-88D for one time step during each event (created using Py-ART; Helmus and Collis 2016), (middle) time-vs-height observations of reflectivity from the MRR during a 4-h period within each event, and (bottom) the precipitation layer depth  $D_{PL}$  in red and delta reflectivity  $\Delta Z$  in black for each event type.

were conducted for relatively short periods of time (i.e., Skofronick-Jackson et al. 2015; Kristovich et al. 2017; Schirle et al. 2019). In this work, we exploit several years of MRR observations from the MQT site through development of an automated snow event classifier. This section outlines both the methodology for the MRR-based snow categorization, and the composited observational results over four winter seasons.

To illustrate the MRR-based categorization for snow events at the MQT site, two snow events from November 2014 are presented. Figure 2 shows WSR-88D base reflectivity plots for a large-scale (top-left panel) and an LES event (top-right panel), using the Py-ART software library (Helmus and Collis 2016). Additionally, we show 4-h time–height plots of the MRR during the large-scale snow event (middle-left panel) and the LES event (middle-right panel). These plots illustrate striking differences: The large-scale snow event is spatially extensive (WSR-88D; top-left panel) and deep (precipitation signature covers the entire observational range of the MRR up to 3000 m AGL) and has high values of relatively constant reflectivities

(from +15 to +20 dBZ). The LES event has banded, convective WSR-88D signatures (top-right panel) and is much shallower (MRR precipitation signature extends to <1500 m AGL), and the reflectivities are pulsed in time and variable (between +5 and +25 dBZ). By using the characteristics of these prototypical examples of large-scale snowfall (deep) and LES (shallow) snow events, the multiyear dataset is categorized in a straightforward manner.

The lower panels in Fig. 2 demonstrate the key MRR products used to determine the deep and shallow snow categories: precipitation layer depth  $D_{PL}$  and delta reflectivity  $\Delta Z$ . To calculate  $D_{PL}$  for any single profile, we count the number of adjacent MRR range gates with observed precipitation (dBZ > -10), beginning with the fourth gate from the ground (400 m AGL). We establish the top of the precipitation layer by the height of the first range gate with no measureable reflectivity, or, alternatively, the highest range gate (at 3000 m AGL). The  $D_{PL}$  is the difference between the top and lowest gate heights of the detected precipitation within the range of

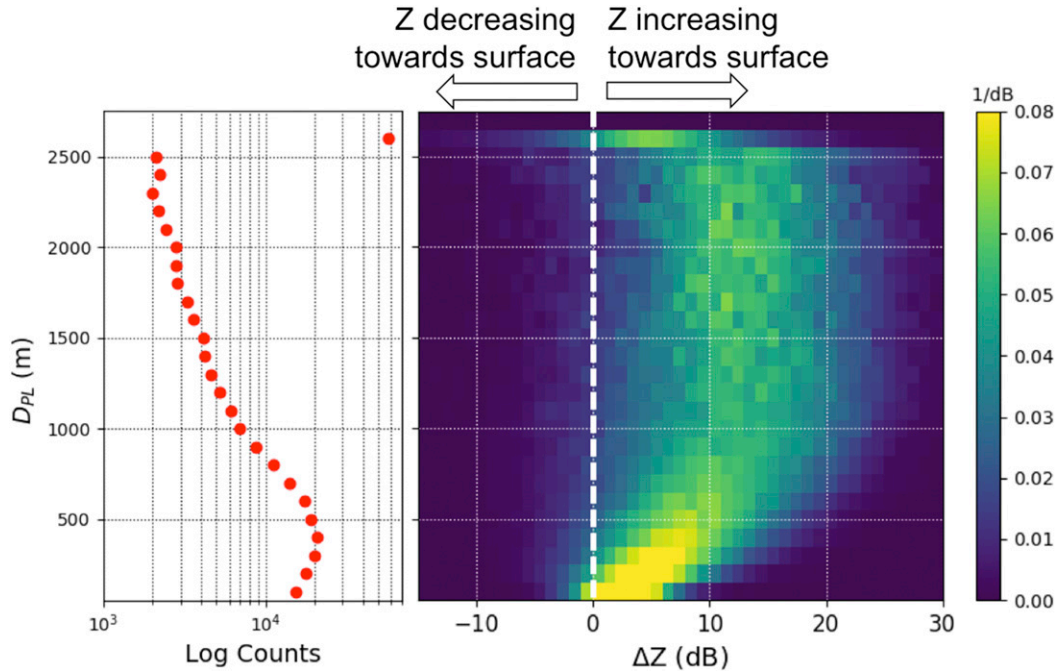


FIG. 3. Compositing MRR information for all of the identified snow events during the winter seasons from 2014 to 2018: (left) The count histogram of  $D_{PL}$  values for all snow events, illustrating the large number of events in the single 2600-m  $D_{PL}$  bin as well as the broad distribution of  $D_{PL}$  values under 1000 m. (right) A CFAD (Yuter and Houze 1995) of all  $D_{PL}$  as a function of the associated  $\Delta Z$ .

usable bins (and therefore does not include the lowest 400 m AGL), and is plotted in red points in the bottom two panels for the large-scale event (left) and the LES event (right). As shown in Fig. 2,  $D_{PL}$  is a constant 2600 m for the large-scale event, while  $D_{PL}$  ranges from  $\sim 700$  to 1100 m for the LES event (lower right). Additionally,  $\Delta Z$  is plotted with a black line (lower panels, Fig. 2).  $\Delta Z$  is the net reflectivity change throughout the MRR-observed precipitating column, calculated by subtracting reflectivity at the top of the measured precipitation layer from the near-surface value (400 m AGL). Since the MRR is only able to observe the precipitation up to 3000 m AGL,  $\Delta Z$  can be used as a metric for examining evolution of the snow in the lower layers of the column. As seen in Fig. 2,  $\Delta Z$  has very different characteristics for the large-scale event (lower left) versus the LES event (lower right): In the large-scale event,  $\Delta Z$  is relatively constant (between 0 and 5 dB) and slowly varying, while in the LES event it varies as much as 20 dB and exhibits a fluctuating pattern.

By using MRR-derived  $D_{PL}$  and  $\Delta Z$  values, we can distill low-level snowfall characteristics and composite large amounts of data into a few demonstrative figures. Figure 3 combines four winter seasons of MRR-derived  $D_{PL}$  and  $\Delta Z$ . We limit the composited MRR observations to the prescribed cold-season months (1 November–30 April) for 2014–2018. In addition, to try to restrict the precipitation

observations to only snowfall, we employ a threshold of  $+2^{\circ}\text{C}$  surface temperature or colder (Bennartz 2007; Liu 2008). The frequency of calculated  $D_{PL}$  during all snow events is illustrated in the left panel of Fig. 3. This illustrates the large number of events in the single 2600-m  $D_{PL}$  bin, a discrete highest count value at the maximum  $D_{PL}$  ( $\sim 56\,000$  counts at 2600 m), as well as the broad distribution of high counts near the surface ( $\sim 140\,000$  counts between 100 and 1500 m). This figure indicates that the majority of the MRR observed snow events are shallow ( $<1500$  m AGL), but many snow events are deep, meaning at or above the highest observed radar bin of 3000 m AGL. Because the limit of the MRR observable range is 3000 m AGL, precipitation processing occurring higher in the atmosphere will be represented in the “deep” category with  $D_{PL} = 2600$  m even though the precipitation likely extends well above that value. It is worth noting that relatively few events occur between 1500- and 2600-m depth ( $<20\,000$  counts). This demonstrates that the four winter seasons of snow events for the MQT site can be broadly cast into either deep ( $D_{PL} = 2600$  m) or shallow ( $D_{PL} < 2600$  m) categories.

In the right panel of Fig. 3, we also relate MRR reflectivities to  $D_{PL}$  and identify differences between deep and shallow snowfall. The left panel of Fig. 3, illustrates the frequency of events as a one-dimensional histogram. The right panel of Fig. 3 is a two-dimensional histogram

in which the frequency of  $\Delta Z$  values are normalized by values of a given  $D_{PL}$  [this method is commonly known as contoured-frequency-by-altitude diagrams (CFAD; Yuter and Houze 1995)]. For shallow snow,  $\Delta Z$  increases for depths up to  $\sim 1000$  m, indicating a potential maximum increase of about 12 dB (Fig. 3, right panel). A positive  $\Delta Z$  roughly implies characteristics of the precipitation microphysical changes within the column, specifically related to growth. Our definition of growth in this context includes the following: an increase in number density of particles (nucleation), larger particle mass (deposition/riming), shifting from smaller to larger average particle size (aggregation), and/or a combination therein. This implies that the shallow snow has greater potential for low-level growth as a function of the layer depth, up to  $\sim 1000$  m. Figure 3 (right panel) illustrates that events at the maximum depth (2600 m) have a smaller  $\Delta Z$ , with  $\sim 5$  dB increase throughout the column, and perhaps indicating less low-level particle growth. The 2600 m  $D_{PL}$  reflectivity distribution is abruptly shifted relative to the rest of the CFAD, due to the fact that this value represents all precipitation at and above the MRR observational range. The implication is that the deep events are markedly different than the shallow events from a particle growth perspective in the lower levels of the precipitation column.

Figure 3 demonstrates that the MRR characteristics associated with the deep events versus shallow events are fundamentally different. Therefore, we can use the information gleaned from the MRR observations as a function of  $D_{PL}$  to partition collocated observations into categories of deep (2600-m depth) and shallow ( $<2600$ -m depth) snow events. This partitioning method allows the surface and profile precipitation microphysical characteristics to be analyzed using both PIP and MRR observations and products. Additionally, the MRR-based partitioning is applied to coincident surface meteorological observations and reanalysis products to examine differences in the associated ambient meteorological conditions and regional influences.

#### 4. Results and discussion

The MRR-based method of partitioning the observed MQT snow events from 2014 to 2018 into deep and shallow categories is applied to the data product described in section 2f. We first discuss the MRR profile observations, WSR-88D echo-top heights, MRR near-surface bin information, and PIP surface products to assess the differences in microphysical characteristics of each snow type. We then evaluate the surface temperature, RH, winds, and pressure measurements, as well as profiles of temperature and RH from reanalyses for each snow type. Last, we compare LWE snowfall accumulation statistics from

the MRR, PIP, and the snow field for the multiyear dataset.

##### a. Microphysical characteristics

###### 1) RADAR OBSERVATIONS

As described in section 3, MRR profile observations are used to separate the snow events into deep (2600-m depth) and shallow ( $<2600$ -m depth) precipitation. Figure 4 shows two-dimensional (2D) histograms of the MRR reflectivity, Doppler velocity, and Doppler spectral width observations for the deep and shallow snow events. The most obvious difference is that observations exist throughout the column for the deep snow events, while the shallow snow event observations are mostly concentrated within the boundary layer. This is not surprising as the MRR-derived  $D_{PL}$  define these categories; however, the shallow events are defined as any events less than 2600-m depth, and it is clear that the vast majority of the observations are below 1500 m AGL (Figs. 4b,d,f). It is again worth emphasizing that there are very few snow events at MQT with precipitation-top heights between 1500 m AGL and the limit of the MRR profiling capabilities (3000 m AGL).

The deep snow events have relatively invariant reflectivity throughout the column (however, there is an indication of a gradient above 2 km), consistent with what was shown in Fig. 3b. These reflectivities tend to range between 0 and 25 dBZ. From examining 2D histograms of individual events (see Fig. S5 in the online supplemental material), we infer that the broad range of reflectivities results from the compositing. In other words, individual deep snow events tend to have a narrow range of reflectivities that are relatively constant (Fig. S5), but that vary significantly between events; therefore, when composited together, the resulting range of reflectivities is broad. In addition, the deep snow events have relatively constant values of Doppler velocity and spectral width throughout the profile (Figs. 4c,e). These values are often greater than  $1 \text{ m s}^{-1}$  and are consistent with radar observations of snow from earlier studies of synoptically driven storm systems (Stark et al. 2013). The 2D histograms of Doppler spectral width (Fig. 4e) have low values throughout the precipitating column, possibly implying lack of turbulence, a narrow range of particle sizes, and/or more similar ice particle habits/shapes.

The shallow events have lower reflectivities on average than the deep events (Fig. 4b), ranging from  $-5$  to 15 dBZ. The shape of the 2D histogram indicates that reflectivity increases closer to the surface during the shallow events, which is consistent with the larger  $\Delta Z$  found in Fig. 3. If we examine 2D histograms of individual LES storms (see Fig. S6 in the online supplemental material), the indication of increasing reflectivities toward the surface is even more



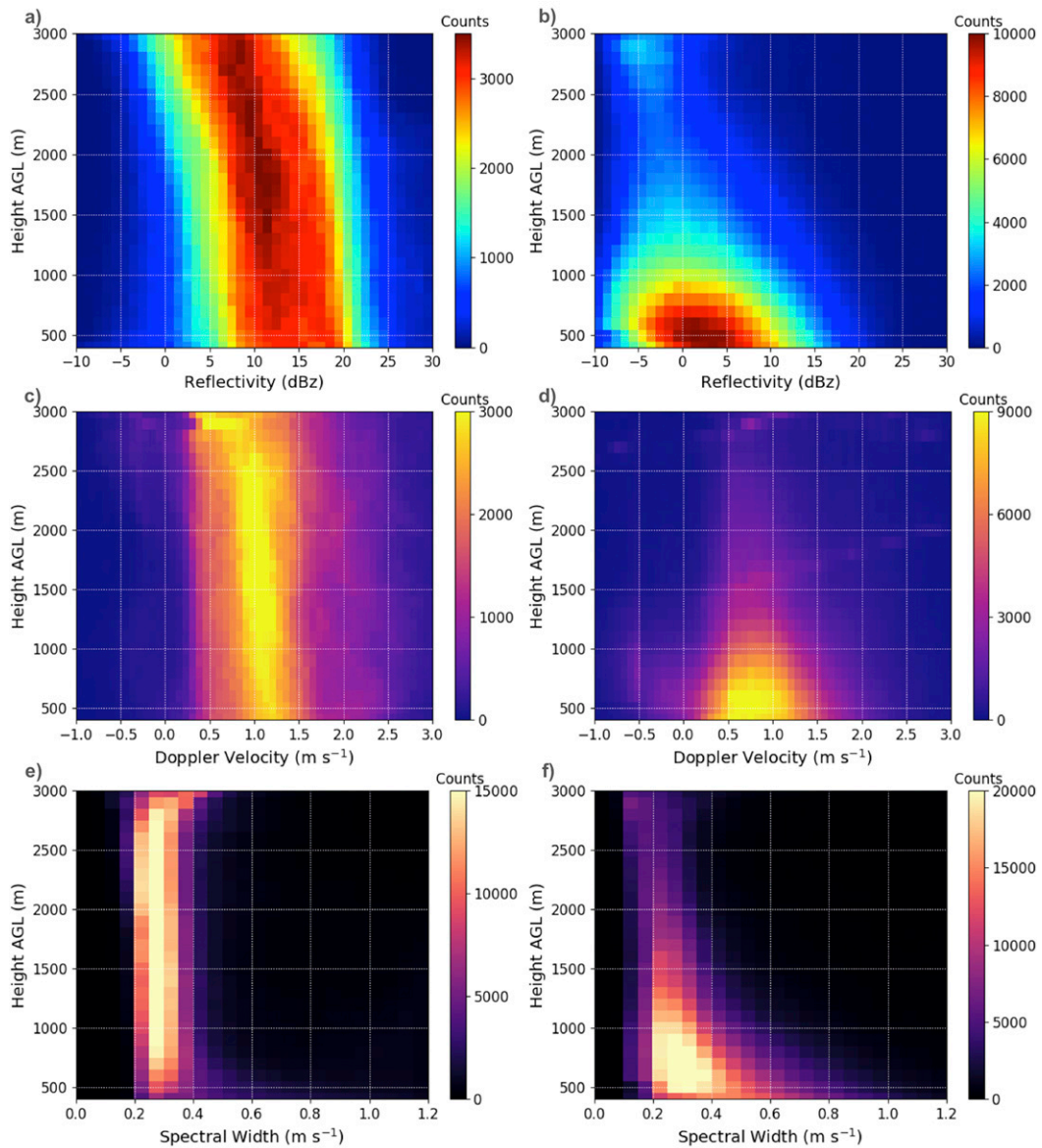


FIG. 4. Two-dimensional histograms of MRR reflectivity for the (a) deep and (b) shallow snow events. The histograms have bins of 100 m for height and 1 dBZ for reflectivity. Two-dimensional histograms of MRR Doppler velocity for the (c) deep and (d) shallow snow events. The histograms have bin widths of 100 m for height and 0.075 m s<sup>-1</sup> for Doppler velocity and 0.05 m s<sup>-1</sup> for Doppler spectral width.

pronounced. The MRR Doppler velocity values for the shallow snow events (Fig. 4d) tend to be less than 1 m s<sup>-1</sup> and vary throughout the column of precipitation (0.5–1 m s<sup>-1</sup>). In addition, the Doppler spectral widths for the shallow snow events (Fig. 4f) are much higher than those for the deep snow events.

Since we are unable to gauge the full depth of the precipitation profiles for the deep snowfall using the MRR, we can utilize WSR-88D EET product to gain further information. In addition, we can examine the shallow event EETs to see if there is general agreement

between precipitation height from the WSR-88D and the MRR. We first examined the WSR-88D VCP operational modes [described in section 2b(2)], as this informs us of the highest scan angle and therefore how close to the site there are EETs above the MRR limits (see Table 2). For the four winter seasons examined (2014–18), the MQT NWS office operated the WSR-88D in VCP 32 for the vast majority of the snow events: 92% of the time for the shallow snow and 65% of the deep. The radar operated in VCP 221 for 35% of the deep and 7% of the shallow events. Therefore, to see

TABLE 2. Details of the WSR-88D VCP scanning mode during the 2014–18 snow events at MQT. Also shown is the frequency of each scanning mode as a function of deep and shallow snowfall.

	VCP 32	VCP 221
Elev tilts	5	9
Max angle	4.3°	19.5°
Deep snow events	65%	35%
Shallow snow events	92%	7%

above the maximum capability of the MRR (3 km AGL), we need to examine the EETs at either  $\geq 15$  km (VCP 221) or  $\geq 50$  km (VCP 32) radial distance from the site.

The mean values of precipitation EET as a function of distance from the radar are shown in Table 3 for the deep and shallow snow. Though the WSR-88D was in the precipitation scanning mode for only 35% of the deep events, we feel that this is a large enough subsample from the four winter seasons of data to glean useful information. The mean EET observed for the deep events was  $\sim 3.6$  km AGL from 15 to 45 km distance from the site (see Table 3) and EETs ranged between 3 and 5 km AGL (figure not shown). The EETs observed for the shallow events tend to agree with the observations from the MRR, with heights ranging from 1 to 1.6 km AGL (see Table 3). Note that since the EETs rely on reflectivities  $\geq 18$  dBZ there will be a bias toward the more intense snow events in this analysis.

In addition to radar-derived information about the snowfall profile and precipitation depth characteristics, we also examined the MRR near-surface (400 m AGL) products. Figure 5 shows the distribution of total counts and normalized counts (with respect to total in each snow category) for the near-surface reflectivity (Figs. 5a and 5b, respectively), Doppler velocity (Figs. 5c and 5d, respectively), and spectral width (Figs. 5e and 5f, respectively). The near-surface reflectivity for the deep snow events is approximately 10 dB higher than the shallow events (mean reflectivity differences between deep and shallow snow are statistically significant). In addition, the range of the near-surface reflectivity observations is broad for each snow category: from  $-7$  to  $+15$  dBZ for the shallow and from  $+2$  to  $+22$  dBZ for the deep events. The near-surface Doppler velocity distributions show higher values for the deep snow events, with a peak at  $\sim 1.3$   $\text{m s}^{-1}$ , while the shallow events generally have lower Doppler velocity values with a maximum at  $\sim 0.7$   $\text{m s}^{-1}$  (mean Doppler velocity differences between deep and shallow snow are statistically significant). In addition, there are negative values of Doppler velocity during the shallow

TABLE 3. Mean EETs for each snow type and WSR-88D VCP scanning mode as a function of radial distance from the MQT NWS site.

Snow event type	Mean EET at 15 km	Mean EET at 30 km	Mean EET at 45 km
Deep (VCP 221)	3.49 km AGL	3.62 km AGL	3.73 km AGL
Shallow (VCP 32)	1.06 km AGL	1.38 km AGL	1.64 km AGL

snow, indicating possible updrafts during these events. The profile of spectral width for the shallow snow events (Fig. 4f) is broader than that of the deep snow events (Fig. 4e), however, the near-surface spectral width ranges are similar (Figs. 5e,f). The near-surface mean spectral width for the deep snow is smaller than the mean for the shallow snow (the difference in means for the spectral width is not statistically significant).

## 2) PIP SURFACE OBSERVATIONS

The PIP observations for each snow category build on the microphysical characteristics gleaned from the MRR presented in the previous section. Figure 6 shows 2D histograms for PIP-derived PSD as a function of the mean particle diameter for the composited deep (Fig. 6, left) and shallow (Fig. 6, center) events. The 2D histograms are normalized by dividing the counts in each bin by the total number counts of the corresponding snow type. The differences between the snow categories are distinct, with a high frequency (0.5%) of small particles (0.4 mm) at  $\geq 10^3$   $\text{m}^{-3} \text{m}^{-1}$  PSD for the deep snow events, while the shallow snow has a broader range of counts for small particles extending across lower PSD values (50–500  $\text{m}^{-3} \text{m}^{-1}$ ), consistent with previous studies (Braham 1990; Barthold and Kristovich 2011). Categorical differencing (Fig. 6, right) reveals the distinct preference for the deep or shallow snow events to contain more or fewer, respectively, small particles (up to  $\sim 8$  mm). In addition, the shallow snow events have a greater concentration of large-diameter particles ( $>10$  mm) than the deep snow events; however, the differences between the deep and shallow PSDs are not statistically significant at  $>6$  mm in diameter.

In addition to looking at the PIP-derived values of PSD, we also examine the shape of the size distribution. Previous studies have applied the following inverse exponential function type to measured snow particle concentrations:

$$N(D) = N_0 \exp(-\Lambda D), \quad (3)$$

where  $N(D)$  is the particle concentration per unit particle size, and  $N_0$  and  $\Lambda$  are the respective PSD intercept

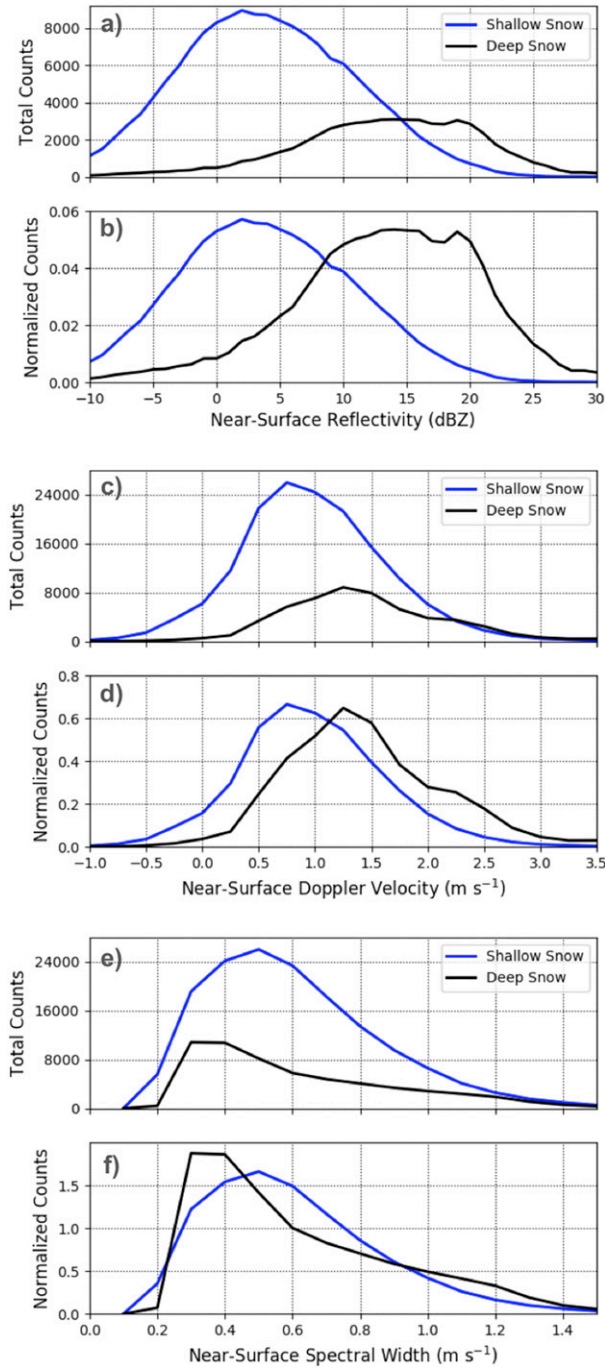


FIG. 5. Histograms of MRR observations from the near-surface (400 m AGL) bin of the deep (black) and shallow (blue) snow events the (a) total and (b) normalized counts of observed MRR reflectivity values using 1-dBZ bin size, (c) total and (d) normalized counts of MRR Doppler velocity observations using  $0.075 \text{ m s}^{-1}$  bin size, and (e) total and (f) normalized counts of the MRR spectral width using  $0.05 \text{ m s}^{-1}$  bin size. The differences in the mean values of reflectivity and Doppler velocity for the deep and shallow snow are significant at the 95% level. The difference in the mean spectral width for the deep and shallow snow events is not statistically significant.

and slope parameters (Lo and Passarelli 1982; Brahm 1990; Heymsfield et al. 2008; Woods et al. 2008). A 15-min running mean was applied to PIP PSD observations to obtain  $N_0$  and  $\Lambda$ . Figure 7 illustrates the normalized composite 2D histograms of  $N_0$  and  $\Lambda$  values for the deep and shallow snow categories (left and middle, respectively). Differences are immediately apparent for each snow category: The deep snow has a high concentration of counts with a large range of  $N_0$  ( $500\text{--}100\,000 \text{ mm}^{-3} \text{ m}^{-1}$ ) and  $\Lambda$  ( $0.4\text{--}2 \text{ mm}^{-1}$ ) values in a tight relationship; while the shallow snow has a bimodal pattern of counts with the highest concentration at very low  $\Lambda$  ( $\sim 0.4 \text{ mm}^{-1}$ ) and  $N_0$  ( $50\text{--}300 \text{ mm}^{-3} \text{ m}^{-1}$ ). As seen in Fig. 7, left, the deep snow events have generally higher  $\Lambda$  values, which indicate narrower PSDs, and larger  $N_0$  values, which imply more small particles (also seen in Fig. 6). The primary mode of the shallow snow events has values of low  $\Lambda$  and  $N_0$  (Fig. 7, center), which indicate broad PSDs with fewer small particles and a higher likelihood of large particles. There is a secondary mode of particle behavior implied in the shallow snow events, with high values of both  $N_0$  ( $\sim 10\,000 \text{ mm}^{-3} \text{ m}^{-1}$ ) and  $\Lambda$  ( $1.6 \text{ mm}^{-1}$ ), which suggest an abundance of small particles with narrow PSDs. This secondary mode may be due to different thermodynamic or physical forcing versus the major mode seen in the shallow snow events. For example, shallow events at the MQT site that occur during extremely cold and windy conditions often produce high numbers of very small particles as observed by the PIP, which would correspond to higher values of  $N_0$  and  $\Lambda$ . The right panel of Fig. 7 illustrates the differences in  $N_0$  and  $\Lambda$  for the snow categories (the shallow subtracted from the deep snow events) with statistically significant differences shown with the black crosses. This figure highlights that the deep snow events have a larger range and higher values of  $N_0$  versus the shallow snow. In addition the deep snow events have narrower PSDs relative to the shallow snow events. In general, most of the shallow snow events have much lower  $N_0$  values and broad PSDs, however, there is a secondary mode of shallow snow production with abundant small particles, distinct from both the deep snow and the majority of the shallow snow events.

*b. Meteorological characteristics*

1) SURFACE WINDS

Figure 8 illustrates the wind roses for the MQT site for all times from 2014 to 2018 (Fig. 8a), during the winter season (Fig. 8b), during deep snow events (Fig. 8c), and during shallow snow events (Fig. 8d). In general, the winter winds tend to look similar to the distribution of the winds for all time; however, there



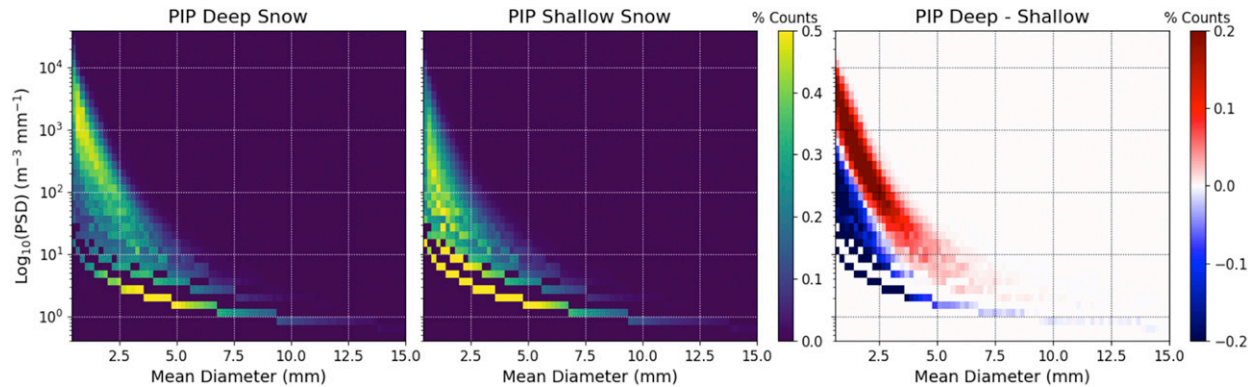


FIG. 6. Composite two-dimensional histograms of PIP observations of PSD as a function of mean diameter of the particles for the (left) deep and (center) shallow snow events, along with (right) the difference of the event types, with red indicating more instances for the deep snow events and blue indicating more instances of shallow events. The discretization of the PIP measured values of PSD and mean diameter is due to the finite measurement volume of the PIP. The differences between the deep and shallow PSDs are significant at 95% up to 6 mm diameter.

is significantly less wind from the south-southwest direction. The pattern of the winds is markedly different between the deep and shallow snow events. Figure 8d shows that the shallow event winds originate broadly out of the west to north-northwest and travel over the lake surface. Since the shallow events are primarily driven by the surface-based lake effect, it is unsurprising that the shallow events are associated with winds that come largely from the direction of Lake Superior. The deep snow events have associated winds with several distinct directions; however, there is a clear dominance from the south-southwest (Fig. 8c) and a preference for winds that originate over land. In general, the wind speeds from the shallow snow events are higher than those associated with the deep snow events.

In Figs. 9 and 10, we have partitioned the winds for each associated snow category by winter month

(November–April). By examining the wind throughout the season, we illuminate patterns that contribute to a distinct snow type. The winds for deep snow events are illustrated in Fig. 9: Deep snow events enhanced by lake interactions (northwest surface winds) and/or orographic effects (northeast surface winds) are more common in the winter shoulder seasons (November and April at MQT). In addition, the deep snow events affiliated with winds from the south-southwest are persistent throughout the winter, with the exception of April where the dominant snow production is from east-northeast. Figure 10 shows a seasonal evolution of the wind patterns associated with the shallow snow events: Early in the winter (November–December), the winds are broadly out of the west to north-northwest, while further into the winter (January–March) the wind distribution is much narrower and generally from the north-northwest. April again experiences a

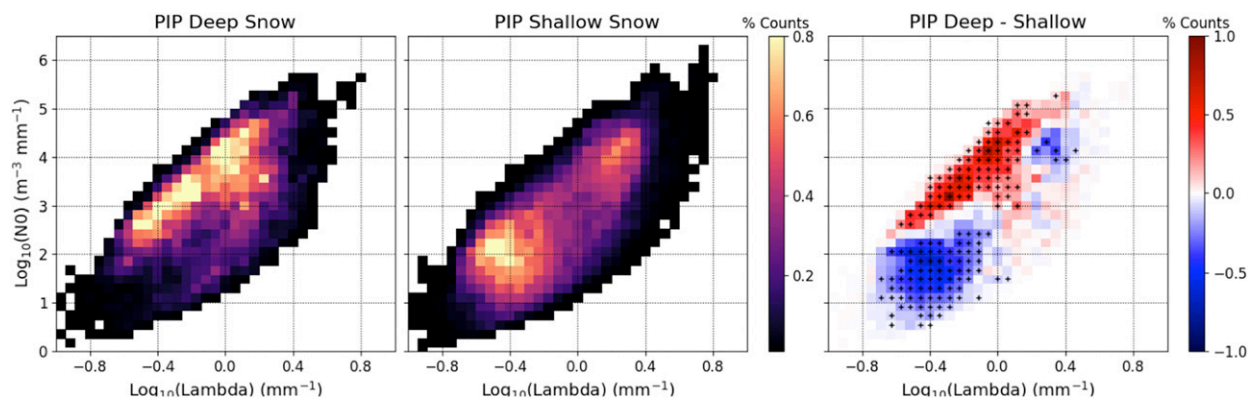


FIG. 7. Similar to Fig. 6, but for PIP products of  $N_0$  as a function of the slope parameter  $\Lambda$ . The black crosses in the right panel indicate where the differences between the deep and shallow snow are significant to 95%.



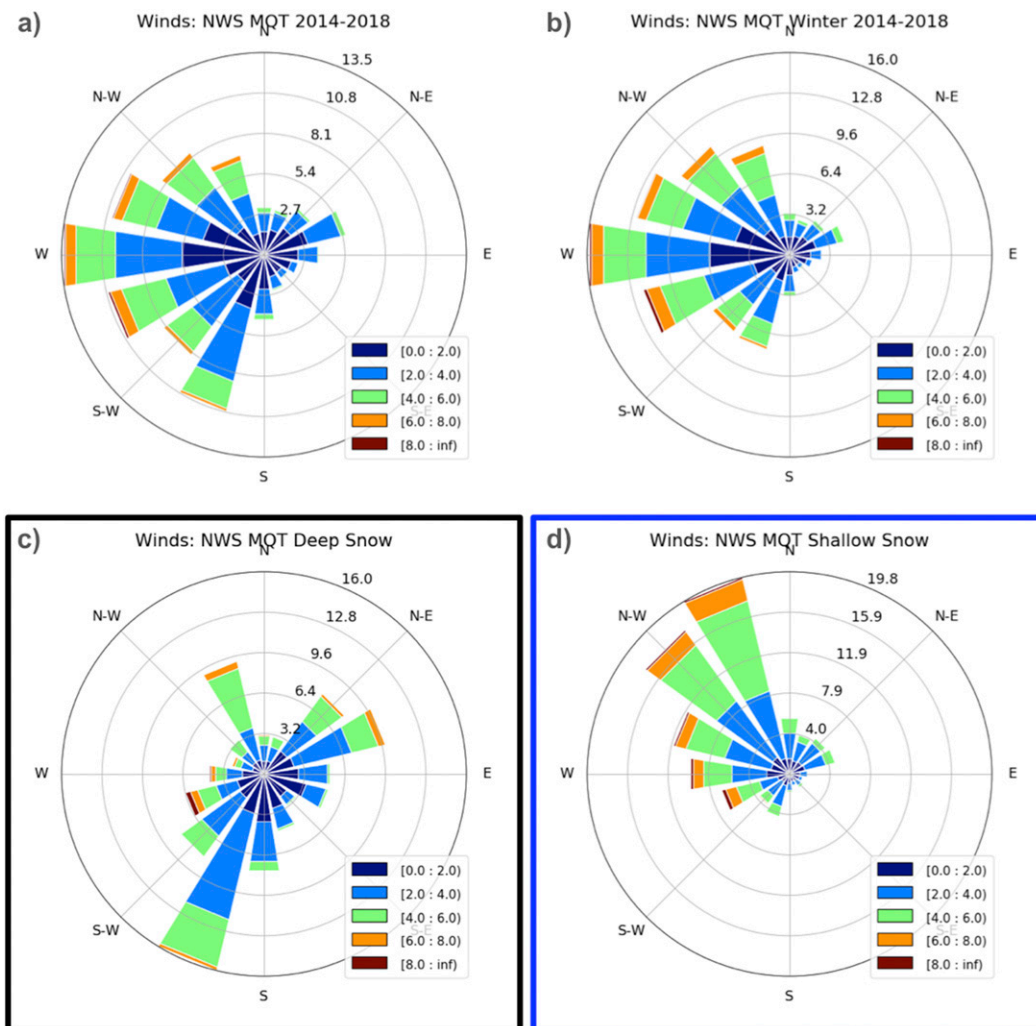


FIG. 8. Surface winds from the MQT office observations (a) for all times from 2014 to 2018, (b) during the winter months of November–April for 2014–18, (c) during MRR-identified deep snow events, and (d) during MRR-identified shallow snow events. The radial axes illustrate the percentage of occurrence of winds binned by direction, and wind speed is indicated by the color bar.

broad wind distribution with a maximum frequency from the north-northwest.

## 2) SURFACE METEOROLOGY AND REANALYSIS PROFILES

Surface temperature, RH, and pressure are shown in Fig. 11, illustrating both the overall distribution (Figs. 11a–c) and the values as a function of month (Figs. 11d–f) for each snow category, correspondingly. In general, the surface temperature (Fig. 11a) and RH (Fig. 11b) values for the deep snow events are higher than those for the shallow snow events. This is also true when examining the distribution broken down by month, with higher temperatures and RH for the deep snow events throughout the winter. The temperature distribution for the deep snow events

peaks near freezing (0°C; Fig. 11a), while the shallow snow events have a mean temperature of approximately −7°C. In general, the deep snow events were coupled to RH greater than 90%, while the shallow snow events had a lower and broader range of values (80%–96%). Figure 11c shows the distribution of the observed surface pressures as a function of snow category. Deep snow events are connected to lower surface pressure, with several peaks in the distribution (around 998, 1007, and 1012 hPa). The shallow snow events have a broad range of surface pressures, but tend to be higher than the deep snow events, regardless of timing throughout the season. The differences in the mean values of temperature and pressure for the deep and shallow snow are statistically significant; however, the difference in means for the RH of the deep and shallow snow is not.

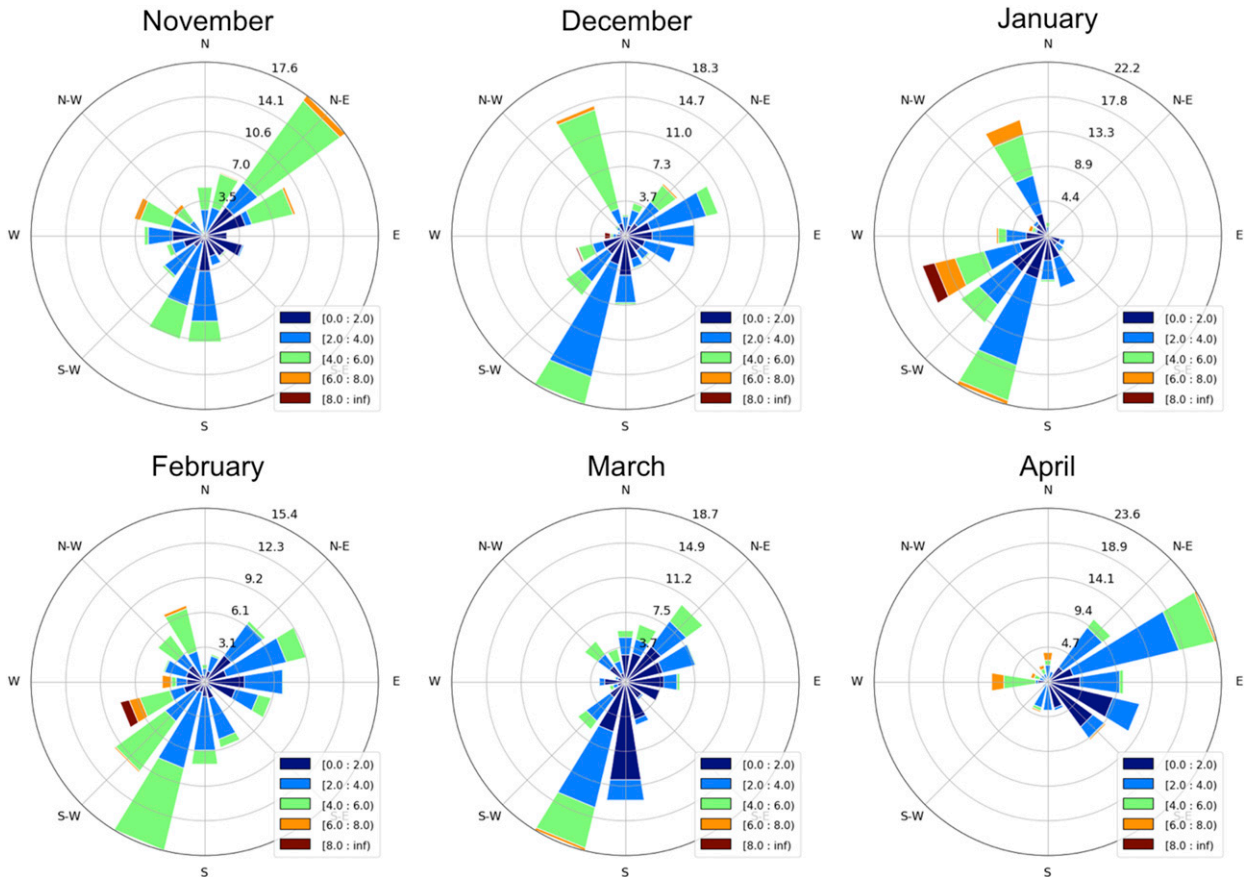


FIG. 9. The winds during the MRR-identified deep snow events from 2014 to 2018 as a function of winter month.

Figure 12 shows profiles of temperature and RH from the ERA5 reanalysis products. In general, the mean temperature profile for the shallow snow events is colder than that for the deep snow events, and surface temperatures are consistent with the measured values from the MQT site. The boundary layer temperature profile for the shallow snow events is colder and ranges between  $-13^{\circ}$  and  $-7^{\circ}\text{C}$ . The temperature profile is on average  $5^{\circ}\text{C}$  warmer and near freezing at the surface for the deep snow events. Lapse rates are reduced at the top of the boundary layer for both snow categories; however, the shallow snow events have a slightly stronger and higher location of a layer of enhanced stability compared to the deep snow events. The differences in the mean values of the temperature profiles are statistically significant, with the exception of 300 hPa. The RH profiles for each snow category are strikingly different, as the free atmosphere above the boundary layer in the shallow snow events is relatively dry (physically consistent with cold-air outbreaks with boundary layer air modified by lake interactions), while the deep snow events are moist ( $>90\%$  RH) throughout up to  $\sim 500$  hPa. Both snow categories have RH values  $> 80\%$  in the boundary

layer, however, the deep snow tends to be higher. There is a maximum RH for the shallow snow at the top of the boundary layer ( $>90\%$  at 850 hPa) and drying throughout the column toward the surface ( $<80\%$ ). This feature strongly hints at a persistent capped boundary layer for the shallow snow cases. The differences in the mean values of the RH profiles are statistically significant everywhere except for 900 and 850 hPa (at the top of the boundary layer in the shallow case).

### c. Microphysical and meteorological discussion

The deep and shallow snow events have both microphysical (MRR indicated) and thermodynamic (reanalysis indicated) profile differences. Additionally, surface observations of microphysics from the PIP and surface meteorological data for each snow category are distinct. These combined profile and surface observational differences imply that separate physical processes drive each snow category. By combining the MRR and PIP observations with the surface meteorology and reanalysis profiles, we can examine characteristics and infer likely processes contributing to snowfall at the surface for each category.

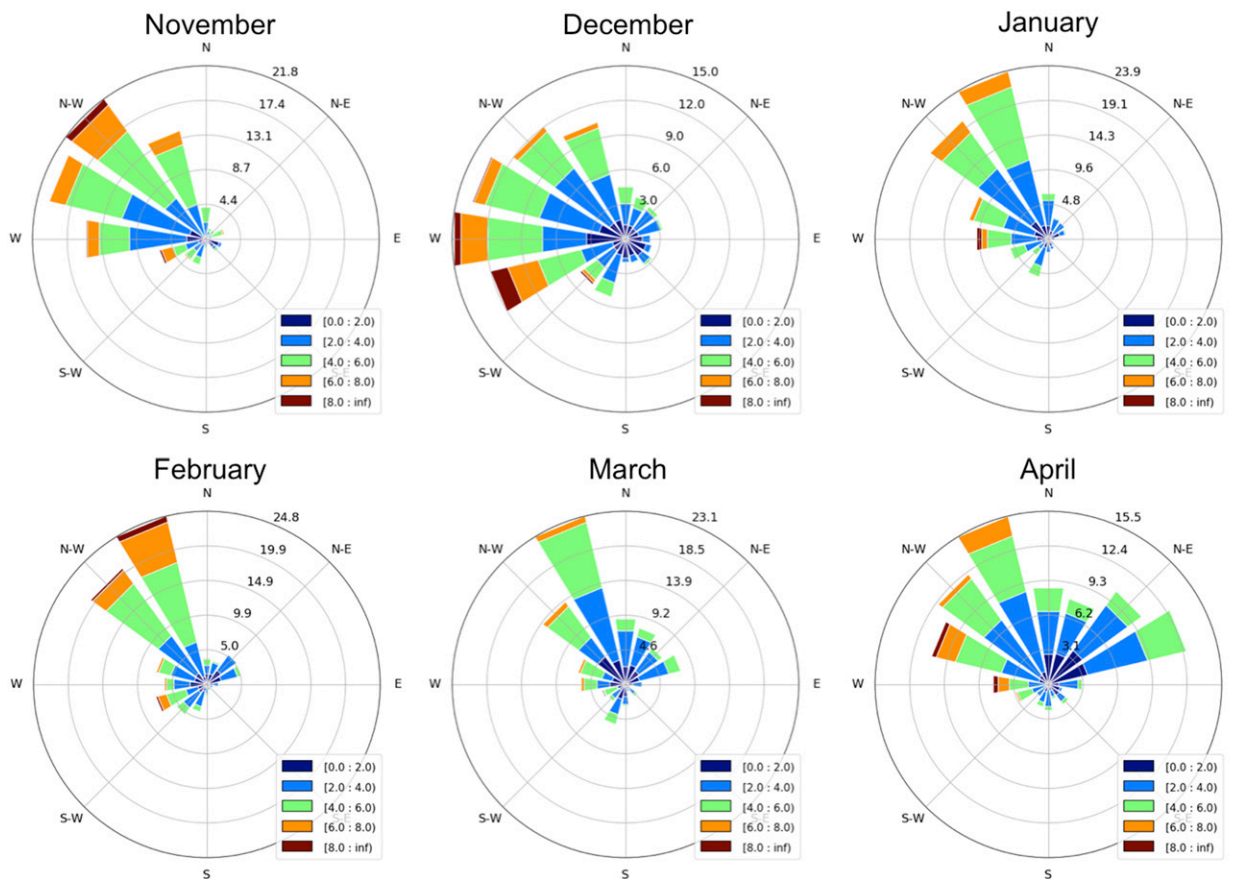


FIG. 10. As in Fig. 9, but for shallow snow events.

### 1) DEEP SNOW

The deep snow events have a maximum wind direction from the south-southwest, and relatively warm surface temperatures (see Fig. 8c). Secondary wind direction maxima occur in the east-northeast, northeast, and north-northwest directions. Synoptic-dynamically driven snowfall production from midlatitude cyclones and attendant frontal structures is associated with warmer temperatures and increased moisture transport into the region (Leathers and Ellis 1996; Serreze et al. 1998). This scenario is supported by the lower surface pressures associated with the deep snow events (see Fig. 11c). The deep snow events coupled to surface winds that traverse over Lake Superior are observed more frequently in November and April, when the lake surface is typically open, which is conducive to lake-enhanced snow that can amplify snow rates (Owens et al. 2017; Kulie et al. 2019, manuscript submitted to *Bull. Amer. Meteor. Soc.*). These lake-enhanced snow events are produced by low-pressure systems that propagate to the southeast and east of Lake Superior and generate winds from the northeast and north directions along the

longest fetch of the lake surface. Orographic enhancement can further inflate snowfall production in deep snow systems under these conditions (Minder et al. 2015; Campbell and Steenburgh 2017). The deep snow events enhanced by lake interactions (northwest to northeast surface winds) and/or orographic effects (typically confined to northeast surface winds) are more common early in the winter season, likely connected to an ice-free Lake Superior (Wang et al. 2012; Kulie et al. 2019, manuscript submitted to *Bull. Amer. Meteor. Soc.*).

The deep snow events tend to be coupled to warmer temperatures and higher relative humidity throughout the atmospheric column when compared to the shallow snow events (Figs. 11 and 12). The high moisture content in the free atmosphere and warmer temperature profiles accompanying the deep snow events are consistent with the larger reflectivities seen in the MRR profile, as the snowfall may have higher ice water content (Yuter and Houze 2003). PIP observations also show higher particle counts in the associated PSDs and  $N_0$  values (Figs. 6 and 7). Although the column mean reflectivity is higher for the

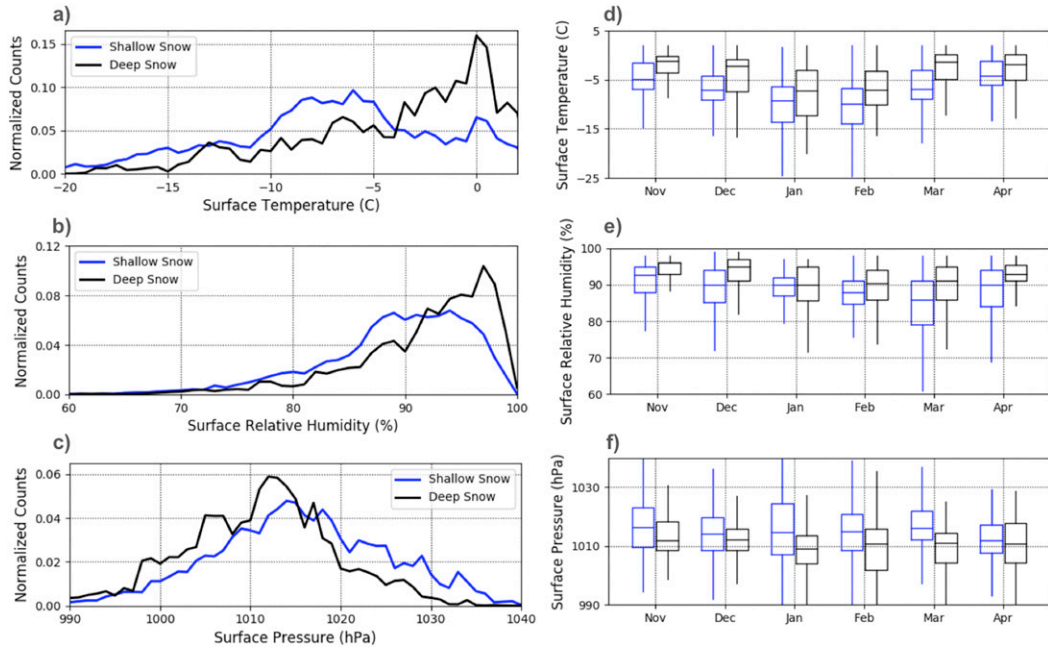


FIG. 11. Several surface meteorological observables are shown for the deep (black) and shallow (blue) snow events illustrated as either (left) one-dimensional histograms of normalized distributions of all of the observations (in total) or (right) as box-and-whisker plots as a function of winter month: (a),(d) surface temperatures (°C), (b),(e) surface RH values (%), and (c),(f) surface pressure (hPa). The box-and-whisker plots illustrate the mean (horizontal line), upper and lower quartiles (top and bottom of box, respectively), and the maximum and minimum (whiskers). The differences in the mean values of temperature and pressure for the deep and shallow snow are significant at the 95% level. The difference in the RH between the deep and shallow snow events is not statistically significant.

deep snow events (see Fig. 3), the reflectivity profile values are relatively invariant below 2000 m AGL (see Fig. 4a). Since the reflectivity profile does not change appreciably in the lower level, this may suggest several processes occurring in the profile below 2000 m AGL: either aggregational

growth ceases, or mean particle size reaches a steady state through complementary particle growth and decay, or the PSD evolves in a way where the reflectivity remains constant (i.e., larger numbers of smaller particles, particle shape/backscattering property changes), or some

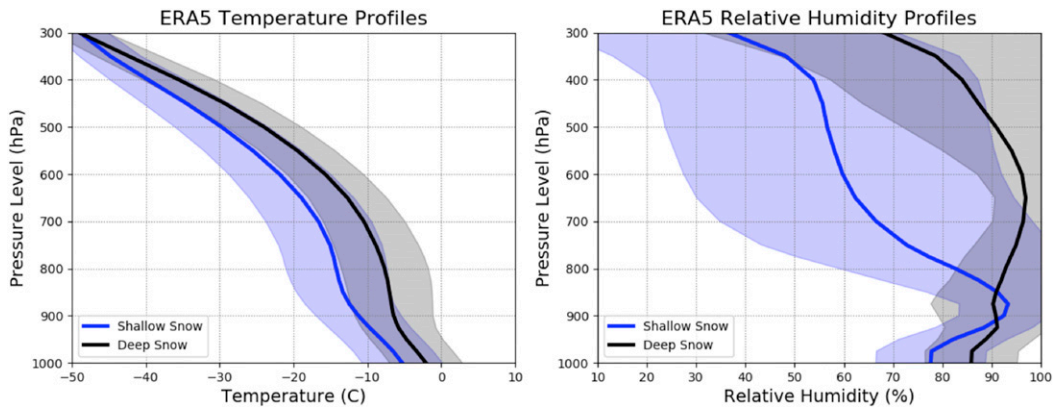


FIG. 12. (left) Temperature and (right) relative humidity profiles from the ERA5 reanalysis. Shallow events are illustrated in blue, and deep events are shown in black. The solid line is the mean, and the shading is 1 standard deviation for the composited events. The differences in the mean values of the temperature profiles are significant at the 95% level with the exception of 300 hPa. The differences in the mean values of the RH profiles are significant at the 95% level everywhere except for 900 and 850 hPa (at the top of the boundary layer in the shallow case).



combination of these effects. Dataset averaging will also attenuate specific deep events where particle growth or decay occurs in the lowest  $\sim 2$  km AGL. The profile of the composite Doppler velocity values for the deep snow events increases between 2000 m AGL and the surface and is similar to those found in studies of synoptic-scale snowstorms (Stark et al. 2013).

The near-surface MRR reflectivities are higher for the deep versus shallow snow events (Fig. 5). This indicates that the deep snow events produce more intense snowfall, meaning either larger mean effective particle diameter, more mass, higher particle density within the observing column, or a combination thereof. This results in a higher radar-retrieved snow rate on average (Atlas et al. 1995; Matrosov et al. 2002). The higher Doppler velocities observed in the near-surface bin for the deep snow events support the notion that the deep snow events contain higher density particles (Atlas et al. 1995; Matrosov et al. 2002; Shupe et al. 2004). The larger  $N_0$  and PSD values are consistent with the higher reflectivity values (and therefore implied snow rate) seen in the MRR observations for the deep snow events, as the PIP observations indicate that more particles are concentrated in the sampling volume (Lo and Passarelli 1982; Atlas et al. 1995; Matrosov et al. 2002; Woods et al. 2008). In general, the observations from the MRR, PIP, and ancillary instrumentation show that the deep snow events are more intense than the shallow snow events at the MQT site.

## 2) SHALLOW SNOW

The shallow snow events are coincident with moderate winds broadly originating from the north and over the surface of Lake Superior, consistent with LES production (Peace and Sykes 1966; Eichenlaub 1979; Niziol et al. 1995). Throughout the winter months, the distribution of wind directions narrows, which may be due to the lake freezing and, consequently, less open water surface area is available to facilitate the boundary layer convection needed to initiate and sustain LES (Wang et al. 2012). Lake Superior generally has ice coverage first from the far western and eastern regions, where the lake is shallow, and last in the center, where the lake is very deep. This pattern of ice formation is linked to the bathymetry of the lake with ice more easily produced over the shallow regions (Assel et al. 2003). Additionally, higher surface pressures and colder surface temperatures accompany the shallow snow events (Fig. 11), consistent with postfrontal cold-air outbreaks over the lake, which often lead to LES production (Agee and Hart 1990).

The reanalysis-based profiles of temperature and RH illustrate key characteristics of LES: Enhanced stability

exists at the top of the boundary layer, which denotes the top of the convection between the surface and the atmosphere (Lavoie 1972); the mean temperature profile in the boundary layer falls in the dendritic growth zone (DGZ; Hallett 1965) range (from  $-12^\circ$  to  $-18^\circ\text{C}$ ), which enables extremely efficient production of snow particle growth (Auer and White 1982; Mitchell 1988); and the ERA5 profile of RH is highest at the top of the boundary layer, which is a characteristic of a well-mixed boundary layer. The location of the maximum mean RH at the top of the boundary layer during the shallow snow events (Fig. 12) suggests that ice crystals initiate and grow similar to mechanisms seen in snow-producing Arctic mixed-phase clouds (Shupe et al. 2006; Morrison et al. 2012). Additionally, the decrease in mean RH throughout the boundary layer indicates sublimation of ice particles below cloud base (where RH is highest) and is consistent with observations from earlier studies of LES snowfall (Barthold and Kristovich 2011; Minder et al. 2015; Campbell and Steenburgh 2017). The high RH and DGZ temperatures in the boundary layer could lead to explosive growth of snow particles and is seen in previous studies of LES and orographic snowfall (Geerts et al. 2011; Minder et al. 2015; Campbell and Steenburgh 2017). Particle growth within the boundary layer is consistent with MRR reflectivity profiles for both individual and composited shallow snow events, as higher reflectivities are located closer to the surface (Figs. 3 and 4). Additionally, the 2D histograms of MRR observations are similar to those in previous MRR-based studies of LES (Minder et al. 2015, Fig. 13) in that the reflectivities generally increase toward the surface in the lowest layers (especially in the inland location in Minder et al. 2015). In Minder et al. (2015), reflectivities for the LES cases are higher ( $\sim 10$ – $15$  dB higher, depending on location) and precipitation layer deeper ( $\sim 2.5$ – $3.5$ -km-layer thickness) than those seen in our shallow events. The Minder et al. (2015) comparisons are not surprising, as we expect the snow at Lake Ontario sites to be more intense than MQT since long-lake-axis-parallel (LLAP) single lake-effect bands commonly affect Lake Ontario. The MQT site typically experiences multi-band, wind-parallel lake-effect events that are less intense than LLAP bands. Furthermore, the MQT site is sheltered by both the Keweenaw Peninsula and Huron Mountains located to the northwest, thus reducing lake fetch for northwest wind lake-effect events.

The Doppler velocity observations for the shallow snow have a broad range throughout the column for both the composite (Figs. 4d and 4f, respectively) and individual events (Fig. S6) and the spectral width values are relatively high compared to the deep events. Together these characteristics suggest turbulent vertical motions in the boundary layer likely associated with

surface-forced convective snowfall processes and are consistent with previous radar-based studies of LES and possibly indicative of turbulence and/or a broader range of particles sizes (Kelly 1982; Kristovich 1993; Yuter and Houze 2003; Welsh et al. 2016). Additionally, negative Doppler velocity values are observed during shallow snow events (Fig. 4d), which may indicate lofting of ice particles by updrafts in the boundary layer, similar to observations from Minder et al. (2015). The implied turbulence within the boundary layer from MRR observations would act as a consistent mechanism to enhance snow particle aggregation and promote particle growth (Lo and Passarelli 1982; Houze and Medina 2005; Geerts et al. 2011). In general, the primary mode of the PSD–diameter and  $N_0$ – $\Lambda$  relationships for shallow snow events (Figs. 6 and 7) indicate there are fewer small particles and more large particles when compared to the deep snow events. Previous work observed below cloud sublimation during a specific LES event (Barthold and Kristovich 2011), which may deplete the population of the small snow particles more than the large and result in fewer small particles observed at the surface. The PIP-derived relationships combined with the relatively lower Doppler velocity values and higher spectral width observations for the shallow snow may indicate that these events tend to consist of fluffy, low-density aggregates. The spectral width range seen during the shallow snow events agree with those seen during an LES event in Minder et al. (2015) for their inland sites. In addition, Minder et al. (2015) observed aggregates of dendrites at both coastal and inland sites, which is consistent with our composite observations of the MQT shallow snow events. Overall, the observations from the MRR, PIP, and ancillary instrumentation show that the shallow snow events are less intense and most snow processes are constrained to the boundary layer and forced by the surface.

#### d. Seasonal occurrence and accumulation

Figure 13 shows the occurrence and accumulation of each snow category as a fraction of the winter total (in LWE) illustrated by month (November–April). Figure 13a shows the MRR-derived occurrence patterns for the deep (black) and shallow (blue) snow as a percentage of winter total. The deep snow occurs evenly, around 4%, for most months, which indicates that midlatitude synoptic systems are fairly regular throughout the winter season. The shallow snow events are more frequent as winter progresses, starting at 8% in November, with a peak of 17% in January, and then tapering to about 7% of the time in April. This pattern is consistent with increasing cold-air outbreaks over the open lake surface in the early winter, followed by progressively more lake ice coverage later in the

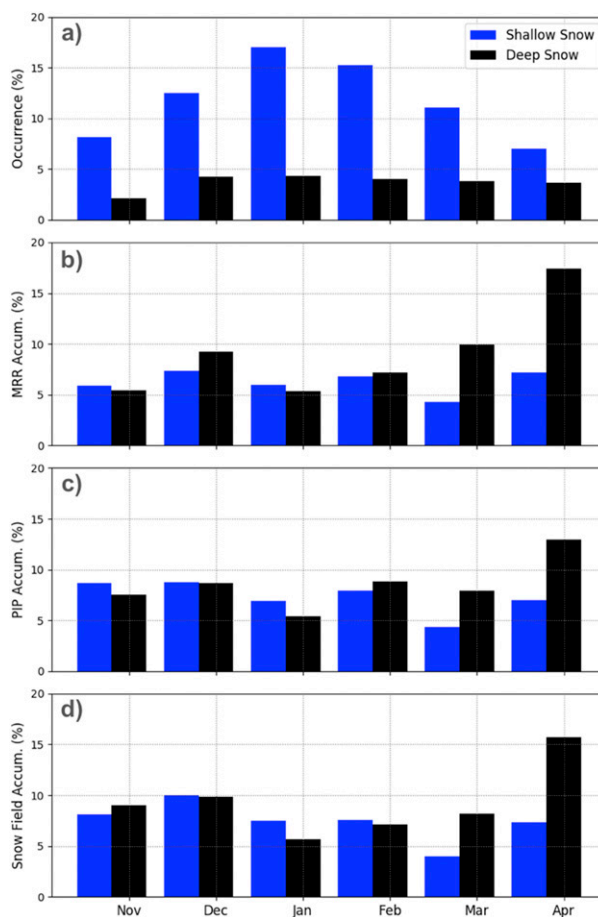


FIG. 13. In each month, the percentage of the total winter snow (a) occurrence (deep in black and shallow in blue), (b) MRR-derived LWE accumulation, (c) PIP-derived LWE accumulation, and (d) NWS snow field LWE accumulation.

winter, thus limiting the amount of LES events. Similar to what was shown in Fig. 3, shallow snow (68%) occurs far more frequently than deep snow (32%).

Figure 13b shows the MRR-derived snow accumulation (LWE; Kneifel et al. 2011; MK12) as a percentage of all snowfall for the four winter seasons. The accumulation pattern is strikingly different from the occurrence—whereas the deep snow happens evenly throughout the winter, the accumulation is highly variable with peaks in December (11%), March (11%), and April (17%). Although the occurrence of shallow snow events grows and then tapers throughout the winter, the accumulation is fairly constant, ranging from 4% to 7% per month. This occurrence pattern reflects lake surface–boundary layer interactions, as less boundary layer moisture may be available as the winter progresses and lake ice cover increases. Using the MRR-derived snow accumulation, the deep (shallow) snow category contributes ~55% (~45%) of all the snowfall at the MQT site.

Figure 13c illustrates the PIP-derived accumulation percentages, which sometimes differ from the MRR-derived values. For instance, the PIP deep snow accumulation during April is only 13%, a  $\sim 4\%$  reduction compared to the MRR estimate. The December deep and shallow accumulation percentages also noticeably change between respective instruments. The prescribed temperature threshold for the MRR snow detection method is  $+2^{\circ}\text{C}$ , whereas the PIP phase partitioning is based on particle velocities, so there may be additional discrepancies at the shoulder seasons. The PIP estimates that deep (shallow) snow events account for  $\sim 51\%$  ( $\sim 49\%$ ) of the overall accumulation.

Figure 13d shows the accumulation percentages obtained from the NWS MQT snow stake field measurements. Each 6-hourly snow field measurement was assigned to the deep or shallow snow event class by computing the relative fractions according to the MRR 1-min observations and selecting based on majority class. As is the case with the MRR and PIP accumulation estimates, April produces the largest accumulations, with  $\sim 15\%$  contribution from deep snow events. The patterns of deep and shallow accumulation ratios as a function of month are similar to those seen by the PIP-derived values. The snow field measurements show that the deep events account for 55% of the accumulation, while the shallow events account for 45%.

## 5. Conclusions

This work highlights the utility of snowfall observations over multiple winter seasons. We are able to illuminate patterns and characteristics of snowfall on the south shore of Lake Superior through strategic deployment of a profiling radar (MRR) and a surface video disdrometer (PIP) with ancillary meteorological observations from the MQT NWS office. By leveraging the MRR profile of reflectivity, we develop a simple metric for partitioning snowfall into deep, system snow events and shallow, largely LES events. Using a merged multiyear dataset, we find that shallow events dominate the frequency of snowfall type (68%) as compared with deep events (32%). However, we find that the deep snow events are much more intense than the shallow snow events, which results in approximately even contribution from each snow type to the overall annual liquid equivalent surface accumulation. By using the collocated PIP surface observations, we find distinct microphysical characteristics of each snowfall type, with the shallow events containing fewer small particles and exhibiting broader PSDs and the deep events containing more small particles and exhibiting narrower PSDs. In addition, by examining the associated

surface meteorological data and available reanalysis profile products with the MRR and PIP observations, we further explore the possible processes contributing to snow particle growth and decay. Comparisons help to illuminate possible snow particle growth process differences in the lower levels of the atmosphere. The shallow snow events experience enhanced growth and aggregation processes likely due to optimal DGZ temperatures and turbulence in the boundary layer. The deep snow events exhibit little to no particle growth in the lowest 2000 m AGL, but contain more mass. Compositing the snow by event type is helpful when examining several seasons of observations. However, this method can obscure some of the more subtle microphysical differences between the deep and shallow snow. A companion study by Kulie et al. (2019, manuscript submitted to *Bull. Amer. Meteor. Soc.*) examines specific snow events in depth and further elucidates key differences in processes.

*Acknowledgments.* We thank the National Weather Service office in Marquette for hosting the instrumentation and sharing meteorological data. To be specific, we thank Robin Turner, David Beachler, Michael Dutter, Todd Kluber, Tim Akom, Gwen Akom, Jim Salzwedel, and Adam Dempsey. We thank colleagues Dan Vimont and Stephanie Henderson for their insight into the appropriate statistical approaches for determining significance. We also thank Marian Mateling for the addition of topography to Fig. 1. Neither the European Commission nor ECMWF is responsible for any use that may be made of the Copernicus information or data it contains. The views, opinions, and findings contained in this paper are those of the authors and should not be construed as an official National Oceanic and Atmospheric Administration or U.S. government position, policy, or decision. This work was funded by the following NASA and NOAA projects: NNX12AQ76G, NNX16AE87G, NNX16AE21G, 80NSSC17K0291, 80NSSC18K0701, 80NSSC19K0712, and NA15NES4320001.

## REFERENCES

- Agee, E. M., and M. L. Hart, 1990: Boundary layer and mesoscale structure over Lake Michigan during a wintertime cold air outbreak. *J. Atmos. Sci.*, **47**, 2293–2316, [https://doi.org/10.1175/1520-0469\(1990\)047<2293:BLAMSO>2.0.CO;2](https://doi.org/10.1175/1520-0469(1990)047<2293:BLAMSO>2.0.CO;2).
- Angel, J. R., and S. A. Isard, 1998: The frequency and intensity of Great Lake cyclones. *J. Climate*, **11**, 61–71, [https://doi.org/10.1175/1520-0442\(1998\)011<0061:TFAIOG>2.0.CO;2](https://doi.org/10.1175/1520-0442(1998)011<0061:TFAIOG>2.0.CO;2).
- Assel, R., K. Cronk, and D. Norton, 2003: Recent trends in Laurentian Great Lakes ice cover. *Climatic Change*, **57**, 185–204, <https://doi.org/10.1023/A:1022140604052>.
- Atlas, D., S. Y. Matrosov, A. J. Heymsfield, M. D. Chou, and D. B. Wolff, 1995: Radar and radiation properties of ice clouds.

- J. Appl. Meteor.*, **34**, 2329–2345, [https://doi.org/10.1175/1520-0450\(1995\)034<2329:RARPOI>2.0.CO;2](https://doi.org/10.1175/1520-0450(1995)034<2329:RARPOI>2.0.CO;2).
- Auer, A. H., Jr., and J. M. White, 1982: The combined role of kinematics, thermodynamics and cloud physics associated with heavy snowfall episodes. *J. Meteor. Soc. Japan*, **60**, 500–507, [https://doi.org/10.2151/JMSJ1965.60.1\\_500](https://doi.org/10.2151/JMSJ1965.60.1_500).
- Barthold, F. E., and D. A. R. Kristovich, 2011: Observations of the cross-lake cloud and snow evolution in a lake-effect snow event. *Mon. Wea. Rev.*, **139**, 2386–2398, <https://doi.org/10.1175/MWR-D-10-05001.1>.
- Bennartz, R., 2007: Passive microwave remote sensing of precipitation at high latitudes. *Measuring Precipitation from Space—EURAINSAT and the Future*, V. Levizziani, J. Turk, and P. Bauer, Eds., Springer, 165–178.
- Braham, R. R., Jr., 1990: Snow particle size spectra in lake effect snows. *J. Appl. Meteor.*, **29**, 200–207, [https://doi.org/10.1175/1520-0450\(1990\)029<0200:SPSSII>2.0.CO;2](https://doi.org/10.1175/1520-0450(1990)029<0200:SPSSII>2.0.CO;2).
- , and M. J. Dungey, 1984: Quantitative estimates of the effect of Lake Michigan on snowfall. *J. Climate Appl. Meteor.*, **23**, 940–949, [https://doi.org/10.1175/1520-0450\(1984\)023<0940:QEOTEO>2.0.CO;2](https://doi.org/10.1175/1520-0450(1984)023<0940:QEOTEO>2.0.CO;2).
- Brown, R. A., T. A. Niziol, N. R. Donaldson, P. I. Joe, and V. T. Wood, 2007: Improved detection using negative elevation angles for mountaintop WSR-88Ds. Part III: Simulations of shallow convective activity over and around Lake Ontario. *Wea. Forecasting*, **22**, 839–852, <https://doi.org/10.1175/WAF1019.1>.
- Burnett, A. W., M. E. Kirby, H. T. Mullins, and W. P. Patterson, 2003: Increasing Great Lake-effect snowfall during the twentieth century: A regional response to global warming? *J. Climate*, **16**, 3535–3542, [https://doi.org/10.1175/1520-0442\(2003\)016<3535:IGLSDT>2.0.CO;2](https://doi.org/10.1175/1520-0442(2003)016<3535:IGLSDT>2.0.CO;2).
- C3S, 2017: ERA5: Fifth generation of ECMWF atmospheric reanalyses of the global climate. Copernicus Climate Change Service Climate Data Store, accessed 19 July 2019, <https://cds.climate.copernicus.eu/cdsapp#!/home>.
- Campbell, L. S., and W. J. Steenburgh, 2017: The OWLeS IOP2b lake-effect snowstorm: Mechanisms contributing to the Tug Hill precipitation maximum. *Mon. Wea. Rev.*, **145**, 2461–2478, <https://doi.org/10.1175/MWR-D-16-0461.1>.
- Casella, D., G. Panegrossi, P. Sanò, A. C. Marra, S. Dietrich, B. T. Johnson, and M. S. Kulie, 2017: Evaluation of the GPM-DPR snowfall detection capability: Comparison with CloudSat-CPR. *Atmos. Res.*, **197**, 64–75, <https://doi.org/10.1016/j.atmosres.2017.06.018>.
- Castellani, B. B., M. D. Shupe, D. R. Hudak, and B. E. Sheppard, 2015: The annual cycle of snowfall at Summit, Greenland. *J. Geophys. Res.*, **120**, 6654–6668, <https://doi.org/10.1002/2015JD023072>.
- Changnon, S. A., Jr., 1979: How a severe winter impacts on individuals. *Bull. Amer. Meteor. Soc.*, **60**, 110–114, [https://doi.org/10.1175/1520-0477\(1979\)060<0110:HASWIO>2.0.CO;2](https://doi.org/10.1175/1520-0477(1979)060<0110:HASWIO>2.0.CO;2).
- Conrick, R., H. D. Reeves, and S. Zhong, 2015: The dependence of QPF on the choice of boundary- and surface-layer parameterization for a lake-effect snowstorm. *J. Appl. Meteor. Climatol.*, **54**, 1177–1190, <https://doi.org/10.1175/JAMC-D-14-0291.1>.
- Davis Instruments, 2018: Wireless Vantage Pro2© and Vantage ©(TM) Plus Stations. Specification sheet DS6152\_62\_53\_63. Rev Z, 12/7/18. Davis Instruments, 10 pp.
- Eichenlaub, V. L., 1979: *Weather and Climate of the Great Lakes Region*. University of Notre Dame Press, 335 pp.
- Geerts, B., Q. Miao, and Y. Yang, 2011: Boundary layer turbulence and orographic precipitation growth in cold clouds: Evidence from profiling airborne radar data. *J. Atmos. Sci.*, **68**, 2344–2365, <https://doi.org/10.1175/JAS-D-10-05009.1>.
- Gorodetskaya, I. V., M. Tsukernik, K. Claes, M. F. Ralph, W. D. Neff, and N. P. Van Lipzig, 2014: The role of atmospheric rivers in anomalous snow accumulation in East Antarctica. *Geophys. Res. Lett.*, **41**, 6199–6206, <https://doi.org/10.1002/2014GL060881>.
- , and Coauthors, 2015: Cloud and precipitation properties from ground-based remote-sensing instruments in East Antarctica. *Cryosphere*, **9**, 285–304, <https://doi.org/10.5194/tc-9-285-2015>.
- Hallett, J., 1965: Field and laboratory observations of ice crystal growth from the vapor. *J. Atmos. Sci.*, **22**, 64–69, [https://doi.org/10.1175/1520-0469\(1965\)022<0064:FALOOI>2.0.CO;2](https://doi.org/10.1175/1520-0469(1965)022<0064:FALOOI>2.0.CO;2).
- Helmus, J. J., and S. M. Collis, 2016: The Python ARM Radar Toolkit (Py-ART), a library for working with weather radar data in the Python programming language. *J. Open Res. Software*, **4**, 25, <https://doi.org/10.5334/jors.119>.
- Henderson, S. A., E. D. Maloney, and E. A. Barnes, 2016: The influence of the Madden-Julian oscillation on Northern Hemisphere winter blocking. *J. Climate*, **29**, 4597–4616, <https://doi.org/10.1175/JCLI-D-15-0502.1>.
- Henne, P. D., F. S. Hu, and D. T. Cleland, 2007: Lake-effect snow as the dominant control of mesic-forest distribution in Michigan, USA. *J. Ecol.*, **95**, 517–529, <https://doi.org/10.1111/j.1365-2745.2007.01220.x>.
- Heymsfield, A. J., P. Field, and A. Bansemmer, 2008: Exponential size distributions for snow. *J. Atmos. Sci.*, **65**, 4017–4031, <https://doi.org/10.1175/2008JAS2583.1>.
- Houze, R. A., and S. Medina, 2005: Turbulence as a mechanism for orographic precipitation enhancement. *J. Atmos. Sci.*, **62**, 3599–3623, <https://doi.org/10.1175/JAS3555.1>.
- Kelly, R. D., 1982: A single Doppler radar study of horizontal-roll convection in a lake-effect snow storm. *J. Atmos. Sci.*, **39**, 1521–1531, [https://doi.org/10.1175/1520-0469\(1982\)039<1521:ASDRSO>2.0.CO;2](https://doi.org/10.1175/1520-0469(1982)039<1521:ASDRSO>2.0.CO;2).
- Klugmann, D., K. Heinsohn, and H. J. Kirtzel, 1996: A low cost 24 GHz FM-CW Doppler radar rain profiler. *Contrib. Atmos. Phys.*, **61**, 247–253.
- Kneifel, S., M. Maahn, G. Peters, and C. Simmer, 2011: Observation of snowfall with a low-power FM-CW K-band radar (Micro Rain Radar). *Meteor. Atmos. Phys.*, **113**, 75–87, <https://doi.org/10.1007/s00703-011-0142-z>.
- Kolka, R. K., C. P. Giardino, J. D. McClure, A. Mayer, and M. F. Jurgensen, 2010: Partitioning hydrologic contributions to an ‘old-growth’ riparian area in the Huron Mountains of Michigan, USA. *Ecohydrology*, **3**, 315–324, <https://doi.org/10.1002/eco.112>.
- Kristovich, D. A., 1993: Mean circulations of boundary-layer rolls in lake-effect snow storms. *Bound.-Layer Meteor.*, **63**, 293–315, <https://doi.org/10.1007/BF00710463>.
- , and Coauthors, 2000: The Lake-Induced Convection Experiment and the Snowband Dynamics Project. *Bull. Amer. Meteor. Soc.*, **81**, 519–542, [https://doi.org/10.1175/1520-0477\(2000\)081<0519:TLCEAT>2.3.CO;2](https://doi.org/10.1175/1520-0477(2000)081<0519:TLCEAT>2.3.CO;2).
- , and Coauthors, 2017: The Ontario Winter Lake-Effect Systems Field Campaign: Scientific and educational adventures to further our knowledge and prediction of lake-effect storms. *Bull. Amer. Meteor. Soc.*, **98**, 315–332, <https://doi.org/10.1175/BAMS-D-15-00034.1>.
- Kulie, M. S., and R. Bennartz, 2009: Utilizing spaceborne radars to retrieve dry snowfall. *J. Appl. Meteor. Climatol.*, **48**, 2564–2580, <https://doi.org/10.1175/2009JAMC2193.1>.
- , and L. Milani, 2018: Seasonal variability of shallow cumuliiform snowfall: A CloudSat perspective. *Quart. J. Roy. Meteor. Soc.*, **144**, 329–343, <https://doi.org/10.1002/QJ.3222>.



- , R. Bennartz, T. J. Greenwald, Y. Chen, and F. Weng, 2010: Uncertainties in microwave properties of frozen precipitation: Implications for remote sensing and data assimilation. *J. Atmos. Sci.*, **67**, 3471–3487, <https://doi.org/10.1175/2010JAS3520.1>.
- , L. Milani, N. Wood, S. Tushaus, R. Bennartz, and T. L'Ecuyer, 2016: A shallow cumuliform snowfall census using spaceborne radar. *J. Hydrometeor.*, **17**, 1261–1279, <https://doi.org/10.1175/JHM-D-15-0123.1>.
- Kunkel, K. E., N. E. Westcott, and D. A. Kristovich, 2002: Assessment of potential effects of climate change on heavy lake-effect snowstorms near Lake Erie. *J. Great Lakes Res.*, **28**, 521–536, [https://doi.org/10.1016/S0380-1330\(02\)70603-5](https://doi.org/10.1016/S0380-1330(02)70603-5).
- Lavoie, R. L., 1972: A mesoscale numerical model of lake-effect storms. *J. Atmos. Sci.*, **29**, 1025–1040, [https://doi.org/10.1175/1520-0469\(1972\)029<1025:AMNMOL>2.0.CO;2](https://doi.org/10.1175/1520-0469(1972)029<1025:AMNMOL>2.0.CO;2).
- Leathers, D. J., and A. W. Ellis, 1996: Synoptic mechanisms associated with snowfall increases to the lee of Lakes Erie and Ontario. *Int. J. Climatol.*, **16**, 1117–1135, [https://doi.org/10.1002/\(SICI\)1097-0088\(199610\)16:10<1117::AID-JOC80>3.0.CO;2-4](https://doi.org/10.1002/(SICI)1097-0088(199610)16:10<1117::AID-JOC80>3.0.CO;2-4).
- Liu, G., 2008: Deriving snow cloud characteristics from *CloudSat* observations. *J. Geophys. Res.*, **113**, D00A09, <https://doi.org/10.1029/2007JD009766>.
- Lo, K. K., and R. E. Passarelli, 1982: The growth of snow in winter storms: An airborne observational study. *J. Atmos. Sci.*, **39**, 697–706, [https://doi.org/10.1175/1520-0469\(1982\)039<0697:TGOSIW>2.0.CO;2](https://doi.org/10.1175/1520-0469(1982)039<0697:TGOSIW>2.0.CO;2).
- Maahn, M., and P. Kollias, 2012: Improved Micro Rain Radar snow measurements using Doppler spectra post-processing. *Atmos. Meas. Tech.*, **5**, 2661–2673, <https://doi.org/10.5194/amt-5-2661-2012>.
- , C. Burgard, S. Crewell, I. V. Gorodetskaya, S. Kneifel, S. Lhermitte, K. Van Tricht, and N. P. van Lipzig, 2014: How does the spaceborne radar blind zone affect derived surface snowfall statistics in polar regions? *J. Geophys. Res. Atmos.*, **119**, 13 604–13 620, <https://doi.org/10.1002/2014JD022079>.
- Matrosov, S. Y., 2007: Modeling backscatter properties of snowfall at millimeter wavelengths. *J. Atmos. Sci.*, **64**, 1727–1736, <https://doi.org/10.1175/JAS3904.1>.
- , A. V. Korolev, and A. J. Heymsfield, 2002: Profiling cloud ice mass and particle characteristic size from Doppler radar measurements. *J. Atmos. Oceanic Technol.*, **19**, 1003–1018, [https://doi.org/10.1175/1520-0426\(2002\)019<1003:PCIMAP>2.0.CO;2](https://doi.org/10.1175/1520-0426(2002)019<1003:PCIMAP>2.0.CO;2).
- Minder, J. R., T. W. Letcher, L. S. Campbell, P. G. Veals, and W. J. Steenburgh, 2015: The evolution of lake-effect convection during landfall and orographic uplift as observed by profiling radars. *Mon. Wea. Rev.*, **143**, 4422–4442, <https://doi.org/10.1175/MWR-D-15-0117.1>.
- Mitchell, D. L., 1988: Evolution of snow-size spectra in cyclonic storms. Part I: Snow growth by vapor deposition and aggregation. *J. Atmos. Sci.*, **45**, 3431–3451, [https://doi.org/10.1175/1520-0469\(1988\)045<3431:EOSSSI>2.0.CO;2](https://doi.org/10.1175/1520-0469(1988)045<3431:EOSSSI>2.0.CO;2).
- Morrison, H., G. De Boer, G. Feingold, J. Harrington, M. D. Shupe, and K. Sulia, 2012: Resilience of persistent Arctic mixed-phase clouds. *Nat. Geosci.*, **5**, 11–17, <https://doi.org/10.1038/ngeo1332>.
- Newman, A. J., P. A. Kucera, and L. F. Bliven, 2009: Presenting the snowflake video imager (SVI). *J. Atmos. Oceanic Technol.*, **26**, 167–179, <https://doi.org/10.1175/2008JTECHA1148.1>.
- Niziol, T. A., 1987: Operational forecasting of lake effect snowfall in western and central New York. *Wea. Forecasting*, **2**, 310–321, [https://doi.org/10.1175/1520-0434\(1987\)002<0310:OFOLES>2.0.CO;2](https://doi.org/10.1175/1520-0434(1987)002<0310:OFOLES>2.0.CO;2).
- , W. R. Snyder, and J. S. Waldstreicher, 1995: Winter weather forecasting throughout the eastern United States. Part IV: Lake effect snow. *Wea. Forecasting*, **10**, 61–77, [https://doi.org/10.1175/1520-0434\(1995\)010<0061:WWFTE>2.0.CO;2](https://doi.org/10.1175/1520-0434(1995)010<0061:WWFTE>2.0.CO;2).
- Norton, D. C., and S. J. Bolsenga, 1993: Spatiotemporal trends in lake effect and continental snowfall in the Laurentian Great Lakes, 1951–1980. *J. Climate*, **6**, 1943–1956, [https://doi.org/10.1175/1520-0442\(1993\)006<1943:STILEA>2.0.CO;2](https://doi.org/10.1175/1520-0442(1993)006<1943:STILEA>2.0.CO;2).
- Notaro, M., A. Zarrin, S. Vavrus, and V. Bennington, 2013: Simulation of heavy lake-effect snowstorms across the Great Lakes basin by RegCM4: Synoptic climatology and variability. *Mon. Wea. Rev.*, **141**, 1990–2014, <https://doi.org/10.1175/MWR-D-11-00369.1>.
- Owens, N. D., R. M. Rauber, B. F. Jewett, and G. M. McFarquhar, 2017: The contribution of lake enhancement to extreme snowfall within the Chicago–Milwaukee urban corridor during the 2011 Groundhog Day blizzard. *Mon. Wea. Rev.*, **145**, 2405–2420, <https://doi.org/10.1175/MWR-D-17-0025.1>.
- Peace, R. L., Jr., and R. B. Sykes Jr., 1966: Mesoscale study of a lake effect snow storm. *Mon. Wea. Rev.*, **94**, 495–507, [https://doi.org/10.1175/1520-0493\(1966\)094<0495:MSOALE>2.3.CO;2](https://doi.org/10.1175/1520-0493(1966)094<0495:MSOALE>2.3.CO;2).
- Peters, G., B. Fischer, and T. Andersson, 2002: Rain observations with a vertically looking Micro Rain Radar (MRR). *Boreal Environ. Res.*, **7**, 353–362, <http://www.borenav.net/BER/pdfs/ber7-353.pdf>.
- Pettersen, C., R. Bennartz, A. J. Merrelli, M. D. Shupe, D. D. Turner, and V. P. Walden, 2018: Precipitation regimes over central Greenland inferred from 5 years of ICECAPS observations. *Atmos. Chem. Phys.*, **18**, 4715–4735, <https://doi.org/10.5194/acp-18-4715-2018>.
- Reeves, H. D., and D. T. Dawson, 2013: The dependence on the choice of microphysical parameterization for lake-effect snowstorms. *J. Appl. Meteor. Climatol.*, **52**, 363–377, <https://doi.org/10.1175/JAMC-D-12-019.1>.
- Rollenbeck, R., J. Bendix, P. Fabian, J. Boy, W. Wilcke, H. Dalitz, M. Oesker, and P. Emck, 2007: Comparison of different techniques for the measurement of precipitation in tropical montane rain forest regions. *J. Atmos. Oceanic Technol.*, **24**, 156–168, <https://doi.org/10.1175/JTECH1970.1>.
- Schirle, C. E., S. J. Cooper, M. A. Wolff, C. Pettersen, N. B. Wood, T. S. L'Ecuyer, T. Ilmo, and K. Nygård, 2019: Estimation of snowfall properties at a mountainous site in Norway using combined radar and in-situ microphysical observations. *J. Appl. Meteor. Climatol.*, **58**, 1337–1352, <https://doi.org/10.1175/JAMC-D-18-0281.1>.
- Schmidlin, T. W., 1993: Impacts of severe winter weather during December 1989 in the Lake Erie snowbelt. *J. Climate*, **6**, 759–767, [https://doi.org/10.1175/1520-0442\(1993\)006<0759:IOSWWD>2.0.CO;2](https://doi.org/10.1175/1520-0442(1993)006<0759:IOSWWD>2.0.CO;2).
- Serreze, M. C., M. P. Clark, D. L. McGinnis, and D. A. Robinson, 1998: Characteristics of snowfall over the eastern half of the United States and relationships with principal modes of low-frequency atmospheric variability. *J. Climate*, **11**, 234–250, [https://doi.org/10.1175/1520-0442\(1998\)011<0234:COSOTE>2.0.CO;2](https://doi.org/10.1175/1520-0442(1998)011<0234:COSOTE>2.0.CO;2).
- Shupe, M. D., P. Kollias, S. Y. Matrosov, and T. L. Schneider, 2004: Deriving mixed-phase cloud properties from Doppler radar spectra. *J. Atmos. Oceanic Technol.*, **21**, 660–670, [https://doi.org/10.1175/1520-0426\(2004\)021<0660:DMCPFD>2.0.CO;2](https://doi.org/10.1175/1520-0426(2004)021<0660:DMCPFD>2.0.CO;2).
- , S. Y. Matrosov, and T. Uttal, 2006: Arctic mixed-phase cloud properties derived from surface-based sensors at SHEBA. *J. Atmos. Sci.*, **63**, 697–711, <https://doi.org/10.1175/JAS3659.1>.
- Skofronick-Jackson, G. M., B. T. Johnson, and S. J. Munchak, 2013: Detection thresholds of falling snow from satellite-borne active and passive sensors. *IEEE Trans. Geosci. Remote Sens.*, **51**, 4177–4189, <https://doi.org/10.1109/TGRS.2012.2227763>.

- , and Coauthors, 2015: Global Precipitation Measurement Cold Season Precipitation Experiment (GCPEX): For measurement's sake, let it snow. *Bull. Amer. Meteor. Soc.*, **96**, 1719–1741, <https://doi.org/10.1175/BAMS-D-13-00262.1>.
- Smalley, M., P. E. Kirstetter, and T. L'Ecuyer, 2017: How frequent is precipitation over the contiguous United States? Perspectives from ground-based and spaceborne radars. *J. Hydrometeor.*, **18**, 1657–1672, <https://doi.org/10.1175/JHM-D-16-0242.1>.
- Sousounis, P. J., and J. M. Fritsch, 1994: Lake-aggregate mesoscale disturbances. Part II: A case study of the effects on regional and synoptic-scale weather systems. *Bull. Amer. Meteor. Soc.*, **75**, 1793–1812, [https://doi.org/10.1175/1520-0477\(1994\)075<1793:LAMDPI>2.0.CO;2](https://doi.org/10.1175/1520-0477(1994)075<1793:LAMDPI>2.0.CO;2).
- , and G. E. Mann, 2000: Lake-aggregate mesoscale disturbances. Part V: Impacts on lake-effect precipitation. *Mon. Wea. Rev.*, **128**, 728–745, [https://doi.org/10.1175/1520-0493\(2000\)128<0728:LAMDPI>2.0.CO;2](https://doi.org/10.1175/1520-0493(2000)128<0728:LAMDPI>2.0.CO;2).
- , —, G. S. Young, R. B. Wagenmaker, B. D. Hoggatt, and W. J. Badini, 1999: Forecasting during the Lake-ICE/SNOWBANDS field experiments. *Wea. Forecasting*, **14**, 955–975, [https://doi.org/10.1175/1520-0434\(1999\)014<0955:FDTLIS>2.0.CO;2](https://doi.org/10.1175/1520-0434(1999)014<0955:FDTLIS>2.0.CO;2).
- Souvereinjs, N., A. Gossart, S. Lhermitte, I. V. Gorodetskaya, S. Kneifel, M. Maahn, F. L. Bliven, and N. P. M. van Lipzig, 2017: Estimating radar reflectivity–Snowfall rate relationships and their uncertainties over Antarctica by combining disdrometer and radar observations. *Atmos. Res.*, **196**, 211–223, <https://doi.org/10.1016/j.atmosres.2017.06.001>.
- , and Coauthors, 2018: Evaluation of the *CloudSat* surface snowfall product over Antarctica using ground-based precipitation radars. *Cryosphere*, **12**, 3775–3789, <https://doi.org/10.5194/tc-12-3775-2018>.
- Stark, D., B. A. Colle, and S. E. Yuter, 2013: Observed microphysical evolution for two East Coast winter storms and the associated snow bands. *Mon. Wea. Rev.*, **141**, 2037–2057, <https://doi.org/10.1175/MWR-D-12-00276.1>.
- Tiira, J., D. N. Moisseev, A. von Lerber, D. Ori, A. Tokay, L. F. Bliven, and W. Petersen, 2016: Ensemble mean density and its connection to other microphysical properties of falling snow as observed in southern Finland. *Atmos. Meas. Tech.*, **9**, 4825–4841, <https://doi.org/10.5194/amt-9-4825-2016>.
- von Lerber, A., D. Moisseev, D. A. Marks, W. Petersen, A. M. Harri, and V. Chandrasekar, 2018: Validation of GMI snowfall observations by using a combination of weather radar and surface measurements. *J. Appl. Meteor. Climatol.*, **57**, 797–820, <https://doi.org/10.1175/JAMC-D-17-0176.1>.
- Wang, J., X. Bai, H. Hu, A. Clites, M. Colton, and B. Lofgren, 2012: Temporal and spatial variability of Great Lakes ice cover, 1973–2010. *J. Climate*, **25**, 1318–1329, <https://doi.org/10.1175/2011JCLI4066.1>.
- Welsh, D., B. Geerts, X. Jing, P. T. Bergmaier, J. R. Minder, W. J. Steenburgh, and L. S. Campbell, 2016: Understanding heavy lake-effect snowfall: The vertical structure of radar reflectivity in a deep snowband over and downwind of Lake Ontario. *Mon. Wea. Rev.*, **144**, 4221–4244, <https://doi.org/10.1175/MWR-D-16-0057.1>.
- Wiggin, B. L., 1950: Great snows of the Great Lakes. *Weatherwise*, **3**, 123–126.
- Wilks, D. S., 2011: *Statistical Methods in the Atmospheric Sciences*. 3rd ed. Elsevier, 676 pp.
- Wood, N. B., T. S. L'Ecuyer, A. J. Heymsfield, and G. L. Stephens, 2015: Microphysical constraints on millimeter-wavelength scattering properties of snow particles. *J. Appl. Meteor. Climatol.*, **54**, 909–931, <https://doi.org/10.1175/JAMC-D-14-0137.1>.
- Woods, C. P., M. T. Stoelinga, and J. D. Locatelli, 2008: Size spectra of snow particles measured in wintertime precipitation in the Pacific Northwest. *J. Atmos. Sci.*, **65**, 189–205, <https://doi.org/10.1175/2007JAS2243.1>.
- Yuter, S. E., and R. A. Houze Jr., 1995: Three-dimensional kinematic and microphysical evolution of Florida cumulonimbus. Part II: Frequency distributions of vertical velocity, reflectivity, and differential reflectivity. *Mon. Wea. Rev.*, **123**, 1941–1963, [https://doi.org/10.1175/1520-0493\(1995\)123<1941:TDKAME>2.0.CO;2](https://doi.org/10.1175/1520-0493(1995)123<1941:TDKAME>2.0.CO;2).
- , and —, 2003: Microphysical modes of precipitation growth determined by S-band vertically pointing radar in orographic precipitation during MAP. *Quart. J. Roy. Meteor. Soc.*, **129**, 455–476, <https://doi.org/10.1256/qj.01.216>.